Time-evolution of ionization and heating around first stars and miniqsos

Rajat M. Thomas[*] and Saleem Zaroubi[*]

Kapteyn Astronomical Institute, Landleven 12, Groningen 9747 AD, the Netherlands

ABSTRACT

A one-dimensional radiative transfer code is developed to track the ionization and heating pattern around the first miniquasars and Population III stars. The code follows the evolution of the ionization of the species of hydrogen and helium and the intergalactic medium temperature profiles as a function of redshift. The radiative transfer calculations show that the ionization signature of the first miniquasars and stars is very similar yet the heating pattern around the two is very different. Furthermore, the first massive miniquasars ($\gtrsim 10^5 \, \mathrm{M_\odot}$) do produce large ionized bubbles around them, which can potentially be imaged directly using future radio telescopes. It is also shown that the ionized bubbles not only stay ionized for considerable time after the switching off of the source, but also continue to expand for a short while due to secondary collisions prompted by the X-ray part of their spectra. Varying spectral shapes also produced sizable variations in ionized fraction and temperature profile. We also compare the radiative transfer results with the analytical approximation usually adopted for heating by miniquasars and find that, because of the inadequate treatment of the He species, the analytical approach leads to an underestimation of the temperature in the outer radii by a factor of ≈ 5. Population III stars – with masses in the range of 10–1000 $\mathrm{M_\odot}$ and modelled as blackbodies at a temperature of 50 000 K – are found to be efficient in ionizing their surroundings. The lack of very high energy photons limits the extent of heating of these first stars and has a distinctly different signature from that of the miniqsos. Observational effects on the 21-cm brightness temperature, the thermal and kinetic Sunyaev–Ze'ldovich effects, are also studied in the context of the upcoming radio and microwave telescopes like LOFAR and SPT.

Key words: quasars: general – cosmology: observations – cosmology: theory – diffuse radiation – radio lines: general.

1 INTRODUCTION

Comprehending the end of the so-called 'dark ages of the Universe' through the process of reionization constitutes a very important step in our understanding of the formation and build-up of structure in the Universe. It also provides a powerful constraint on various cosmological models (Tozzi et al. 2000; Zaldarriaga, Furlanetto & Hernquist 2004; Bharadwaj & Ali 2005). Observation of this crucial epoch in the history of the Universe is possible through the redshifted 21-cm emission from neutral hydrogen as first recognized by Sunyaev & Ze'ldovich (1975) and further improved upon and developed by many authors like Hogan & Rees (1979), Scott & Rees (1990) and Madau, Meiksin & Rees (1997).

One of the popular views on how reionization occurred is the following (Furlanetto, Zaldarriaga & Hernquist 2004a); first sources of light, be it Population III (hereafter Pop III) stars, miniquasars or

any other source of radiation, created ionized bubbles. These ionized bubbles probably started to form around high density peaks, roughly at the same time, everywhere in the Universe. As the sources number increased and since the expansion rate of these bubbles was greater than the Universe's expansion, the bubbles overlapped around a certain redshift. A novel class of large radio telescopes like LO-FAR,[1] MWA,[2] 21CMA[3] and SKA[4] is being designed, among other things, to map the 21-cm emission from neutral diffuse Intergalactic Medium (IGM) at the Epoch of Reionization (EoR) as a function of redshift, where they will detect the statistical signature of the high-redshift Universe as a function of z (Furlanetto, Zaldarriaga & Hernquist 2004b; Zaldarriaga et al. 2004). The ultimate goal of these mega radio telescopes would lie in resolving and mapping

---

[1] www.lofar.org; www.astro.rug.nl/~LofarEoR
[2] http://www.haystack.mit.edu/ast/arrays/mwa/
[3] http://21cma.bao.ac.cn/
[4] www.skatelescope.org

[*]E-mail: thomas@astro.rug.nl (RMT); saleem@astro.rug.nl (SZ)

the ionized bubbles and their evolution around the first sources of ultraviolet (UV) radiation.

Recent observations show that quasars with black hole masses as large as $10^9\,M_\odot$ have already existed at a redshift of 6 and higher (Fan et al. 2003, 2006) suggesting the existence of miniquasars that harbour intermediate mass black holes with masses in the range of $10^{3-6}\,M_\odot$ at very high redshifts ($z > 10$). A scenario in which a black hole starts accreting mass at very high redshift thus producing UV and X-ray radiation that ionizes and heats up its surrounding IGM has been studied by many authors (Furlanetto & Loeb 2002; Dijkstra et al. 2004; Furlanetto et al. 2004b; Ricotti & Ostriker 2004a,b; Wyithe & Loeb 2004; Nusser 2005). Many aspects of the above scenario are debatable, e.g. what was the primordial black hole formation mechanism (Begelman, Volonteri & Rees 2006; Spaans & Silk 2006) and what was the evolution rate of their mass densities as a function of redshift which varies dramatically depending on the model used (cf. Begelman et al. 2006; Rhook & Haehnelt 2006; Zaroubi et al. 2007, for different scenarios)? Furthermore, the spectral indices of the power-law spectral energy distribution of a quasar, even if marginally different, can suggest very different imprints. Also the accretion rate and lifetimes of these primordial objects are completely unknown.

Apart from these large potential variations in parameters within the scenario of miniqsos, we also have the distinctively different scenario of Pop III stars as the primary source of reionization (Barkana & Loeb 2001; Bromm, Kudritzki & Loeb 2001; Ciardi, Ferrara & White 2003; Wyithe & Loeb 2003; Kitayama et al. 2004; Whalen, Abel & Norman 2004; Benson et al. 2006; Chen & Miralda-Escude 2006; Loeb 2006; Abel, Wise & Bryan 2007). Within the context of Pop III stars, there are many uncertainties that need to be considered. For example, the unknown blackbody temperature of the star (assuming they can be characterized by one) its mass, lifetimes, clustering properties and redshifts at which they start to appear.

In this paper, we try to fully explore the implications of varying the above mentioned parameters on the final maps of the 21-cm signal for individual objects that are initially surrounded by neutral IGM. In order to achieve a full sample of this parameter space it becomes imperative that a fast and realistic method of modelling these parameters is introduced. Previous simulations of radiative transfer (RT) in cosmological context and studies on the impact of first sources on the surrounding IGM, show that the regions that are ionized around these first sources, are almost spherically symmetric, e.g. fig. 7 of Kuhlen & Madau (2005). Thus, we resorted to developing and using a one-dimensional RT code to study the ionizing fronts (I-front) their velocity, size, shape and so on.

Quick execution times and the simplicity in setting up the initial conditions allow us to simulate the influence of the miniquasars with varying masses for different redshifts, lifetimes and spectral indices. Specifically, we explore the influence of individual black hole masses ranging from 100 to $10^8\,M_\odot$, redshifts between 10 and 30 and lifetimes in the range of 3–20 Myr. The influence of first stars on the IGM was explored with mass ranges of 10–$10^3\,M_\odot$, whose luminosity is determined mainly by their mass (Schaerer 2002).

The upcoming radio telescopes like LOFAR, MWA, 21CMA and SKA will be used to observe the redshift of 21 cm from the dark ages and the EoR. Hence, trying to predict the topology, intensity and distribution of the ionized regions as a function of redshift is crucial in the development of sophisticated data analysis techniques to retrieve the 21-cm EoR signal. Given the spatial resolution of these radio telescopes, it is very hard to differentiate between the ionization bubbles around miniqsos and Pop III stars. Chen & Miralda-Escude (2006), Kuhlen & Madau (2005) and Zaroubi & Silk (2005) have

suggested ways to differentiate between various sources of ionization. In this paper, it is shown that the heating caused by these two possible ionization sources is significantly different especially at the early stages of the EoR, leading to different strengths of coupling between the spin and kinetic temperature which is reflected in the measured brightness temperature. Therefore, we argue that this feature could, in principle, be used to distinguish between ionization sources.

The paper is structured as follows. In Section 2, we detail the rate equations used in the simulations and also describe how we solve for the radial dependencies of the ionized fractions of the various species involved and of the temperature. Accuracy and reliability of the RT code developed were tested. Results of the two tests conducted, namely, propagation of the ionizing front into the mean non-expanding IGM and the Shapiro & Giroux case in which the IGM is expanding with the Universe, are presented in Section 3. Section 4 outlines some of the results obtained in the application of this code to power-law sources. A similar exercise is carried out for the case of stars, and results discussed in Section 5. The coupling mechanisms between the spin and kinetic temperatures and its effect on the brightness temperature is discussed in Section 6. Other observables like the thermal and kinetic Sunyaev–Ze'ldovich (SZ) effects caused by these sources are considered in Section 7. We present our conclusions and the possibilities of expanding this work further in Section 8. We also present a comparison of the heating profiles provided by the code developed here with an analytical approach developed earlier in the Appendix A.

2 SIMULATIONS

The results presented in this study are based on a one-dimensional RT code with which the evolution of H I, H II, He I, He II, He III, free electrons and temperature is monitored on time. In order to achieve this, we follow Fukugita & Kawasaki (1994), wherein a set of coupled differential equations (1–3 and 12) are solved . We follow Jones & Wyse (1985) and Fukugita & Kawasaki (1994) in treating hydrogen as two level system plus a continuum.

For this study, in the case of miniqsos, we simply assumed that the density surrounding it is the mean density in an expanding Universe. For the case of stars, we assume an isothermal like profile of the form $\rho(r)\,(\mathrm{cm}^{-3}) = 3.2(91.5\,\mathrm{pc}/r)^2$, as in Mellema et al. (2006), until the density reaches the mean IGM density, after which we set the density to that of the mean IGM. The cosmological parameters used here are those set by the WMAP third year results (Spergel et al. 2007).

2.1 Rate equations

In the RT code we developed, the radiation is allowed to propagate radially with an underlying density profile, which in our case is the constant background IGM density. The code solves the following rate equations and finds the number density of each species in time and space:

$$\frac{\mathrm{d}n_{\mathrm{H\,II}}}{\mathrm{d}t} = \Gamma_{\mathrm{H\,I}}n_{\mathrm{H\,I}} - \alpha_{\mathrm{H\,II}}n_{\mathrm{e}}n_{\mathrm{H\,II}}, \tag{1}$$

$$\begin{aligned}
\frac{\mathrm{d}n_{\mathrm{He\,II}}}{\mathrm{d}t} = &\;\Gamma_{\mathrm{He\,I}}n_{\mathrm{He\,I}} - \beta_{\mathrm{He\,I}}n_{\mathrm{e}}n_{\mathrm{He\,I}} \\
&+ \beta_{\mathrm{He\,II}}n_{\mathrm{e}}n_{\mathrm{He\,II}} - \alpha_{\mathrm{He\,II}}n_{\mathrm{e}}n_{\mathrm{He\,II}} \\
&+ \alpha_{\mathrm{He\,III}}n_{\mathrm{e}}n_{\mathrm{He\,III}} - \xi_{\mathrm{He\,II}}n_{\mathrm{e}}n_{\mathrm{He\,II}},
\end{aligned} \tag{2}$$

$$\frac{\mathrm{d}n_{\mathrm{He\,III}}}{\mathrm{d}t} = \Gamma_{\mathrm{He\,II}}n_{\mathrm{He\,II}} - \beta_{\mathrm{He\,II}}n_{\mathrm{e}}n_{\mathrm{He\,II}}$$
$$+ \alpha_{\mathrm{He\,III}}n_{\mathrm{e}}n_{\mathrm{He\,III}}, \tag{3}$$

$$\Gamma_{\mathrm{H\,I}} = \gamma_{2\mathrm{c}} + \beta_{\mathrm{H\,I}}n_{\mathrm{e}} + \int_{E_{\mathrm{H\,I}}}^{\infty} \sigma_{\mathrm{H\,I}}N(E;r;t)\frac{\mathrm{d}E}{E}$$
$$+ f_{\mathrm{H}}\left[\int_{E_{\mathrm{H\,I}}}^{\infty} \sigma_{\mathrm{H\,I}}\left(\frac{E-E_{\mathrm{H\,I}}}{E_{\mathrm{H\,I}}}\right)N(E;r;t)\frac{\mathrm{d}E}{E}\right]$$
$$+ f_{\mathrm{H}}\left[\frac{n_{\mathrm{He\,I}}}{n_{\mathrm{H\,I}}}\int_{E_{\mathrm{He\,I}}}^{\infty} \sigma_{\mathrm{He\,I}}\left(\frac{E-E_{\mathrm{He\,I}}}{E_{\mathrm{H\,I}}}\right)N(E;r;t)\frac{\mathrm{d}E}{E}\right], \tag{4}$$

$$\Gamma_{\mathrm{He\,I}} = \int_{E_{\mathrm{He\,I}}}^{\infty} \sigma_{\mathrm{He\,I}}N(E;r;t)\frac{\mathrm{d}E}{E}$$
$$+ f_{\mathrm{He}}\left[\int_{E_{\mathrm{He\,I}}}^{\infty} \sigma_{\mathrm{He\,I}}\left(\frac{E-E_{\mathrm{He\,I}}}{E_{\mathrm{He\,I}}}\right)N(E;r;t)\frac{\mathrm{d}E}{E}\right]$$
$$+ f_{\mathrm{He}}\left[\frac{n_{\mathrm{H\,I}}}{n_{\mathrm{He\,I}}}\int_{E_{\mathrm{He\,I}}}^{\infty} \sigma_{\mathrm{H\,I}}\left(\frac{E-E_{\mathrm{H\,I}}}{E_{\mathrm{He\,I}}}\right)N(E;r;t)\frac{\mathrm{d}E}{E}\right], \tag{5}$$

$$\Gamma_{\mathrm{He\,II}} = \int_{E_{\mathrm{He\,II}}} \sigma_{\mathrm{He\,II}}N(E;r;t)\frac{\mathrm{d}E}{E}, \tag{6}$$

where $n_{\mathrm{H\,I}}$, $n_{\mathrm{H\,II}}$, $n_{\mathrm{He\,I}}$, $n_{\mathrm{He\,II}}$ and $n_{\mathrm{He\,III}}$ are the neutral and ionized hydrogen, neutral, single and doubly ionized helium densities, respectively. n_{e} is the total electron density given by $n_{\mathrm{e}} = n_{\mathrm{H\,II}} + n_{\mathrm{He\,I}} + 2n_{\mathrm{He\,II}}$, $E_{\mathrm{H\,I}}$, $E_{\mathrm{He\,I}}$ and $E_{\mathrm{He\,II}}$ are the ionization energies for the corresponding species. β are the collisional ionization coefficients, α and ξ, the recombination coefficients, σ are the bound–free photoionization cross-sections, $\gamma_{2\mathrm{c}} = \alpha_{\mathrm{H\,I}}(T_{\gamma})(m_{\mathrm{e}}kT_{\gamma}/2\pi)^{3/2}\mathrm{e}^{-3.4\,\mathrm{eV}/T_{\gamma}}$, is the photoionization coefficient due to background photons. The subscripts denote the species to which the coefficient belongs.

The radiation flux $N(E;r;t)$ is the same as in Zaroubi & Silk (2005):

$$N(E;r;t) = \mathrm{e}^{-\tau(E;r;t)}\frac{Ag}{(r/\mathrm{Mpc})^2}I(E) \quad \left(\mathrm{cm}^{-2}\,\mathrm{s}^{-1}\right), \tag{7}$$

where $I(E)$ is the spectral energy distribution, Ag, is the normalization coefficient calculated as

$$Ag = \frac{E_{\mathrm{total}}}{\int_{E_{\mathrm{range}}} I(E)\,\mathrm{d}E}, \tag{8}$$

where E_{total} is the total energy output of the *first* objects within the energy range (E_{range}) and the optical depth $\tau\,(E;r;t)$ is given by

$$\tau(E;r;t) = \sum_{\mathrm{i}} \int_r \sigma_{\mathrm{i}}(E)n_{\mathrm{i}}(r;t)\,\mathrm{d}r, \tag{9}$$

where the sum is over all species. The effects of secondary ionizations – due to the kinetic energy carried by ejected electron – have been folded in through the terms f_{H} and f_{He}. These two terms depend on the ionization state of the medium and given by (Shull & van Steenberg 1985)

$$f_{\mathrm{H}} = 0.3908\left(1 - x_{\mathrm{ion}}^{0.4092}\right)^{1.7592} \tag{10}$$

and

$$f_{\mathrm{He}} = 0.0554\left(1 - x_{\mathrm{ion}}^{0.4614}\right)^{1.6660}. \tag{11}$$

Here, x_{ion} is the ionized fraction of hydrogen. For ionization, this effect becomes significant when dealing with very high-energy (HE) photons (>1 KeV) and when the medium is neutral to partially ionized.

Note here that the causality aspect of the code comes in through the ionization terms. Because, as will be discussed later, we are presenting a grid code in which the memory of the ionization history of all the cells prior to the cell under consideration is embedded in the optical depth, which in turn dictates the amount of radiation available to ionize a particular cell.

Fits for the collisional ionization and recombination coefficients were obtained from the appendix of Fukugita & Kawasaki (1994). The photoionization cross-sections though are obtained using the fitting formula of Verner et al. (1996). For the exact form of these fitting function, we refer the reader to these two papers.

The temperature evolution is monitored by coupling equations (1)–(3) with the equation below:

$$\frac{3}{2}\frac{\mathrm{d}}{\mathrm{d}t}\left(\frac{kT_{\mathrm{e}}n_{\mathrm{B}}}{\mu}\right)$$
$$= f_{\mathrm{Heat}}\sum_{i=\mathrm{H\,I,He\,I,He\,II}}n(i)\int \sigma_{\mathrm{i}}(E-E_{\mathrm{i}})N(E;r;t)\frac{\mathrm{d}E}{E}$$
$$+ \frac{\sigma_{\mathrm{s}}n_{\mathrm{e}}}{m_{\mathrm{e}}c^2}\sum_{i=\mathrm{H\,I,He\,I,He\,II}}\int N(E;r;t)(E-4k_{\mathrm{B}}\mathrm{T})\,\mathrm{d}E$$
$$- \sum_{i=\mathrm{H\,I,He\,I,He\,II}}\zeta_{\mathrm{i}}n_{\mathrm{e}}n(i)$$
$$- \sum_{i=\mathrm{H\,II,He\,II,He\,III}}\eta_{\mathrm{i}}n_{\mathrm{e}}n(i)$$
$$- \omega_{\mathrm{He\,II}}n_{\mathrm{e}}n_{\mathrm{He\,III}}$$
$$- \sum_{i=\mathrm{H\,I,He\,I,He\,II}}\psi_{\mathrm{i}}n_{\mathrm{e}}n(i)$$
$$- \theta_{ff}(n_{\mathrm{H\,II}} + n_{\mathrm{He\,II}} + 4n_{\mathrm{He\,III}})n_{\mathrm{e}}$$
$$- 2\frac{\dot{a}}{a}\left(\frac{kT_{\mathrm{e}}n_{\mathrm{B}}}{\mu}\right). \tag{12}$$

The form of equation (12) is identical to that of Fukugita & Kawasaki (1994) except for the inclusion of the Compton heating term (Madau & Efstathiou 1999) which becomes important as we approach the source which is placed at the centre, i.e. radius equals to zero. In the above equation, E_{i} is the threshold energy of ionization of the ith species which is either H I, He I or He II. σ_{s} is the Thompson scattering cross-section of an electron ($\sigma_{\mathrm{s}} = 6.6524 \times 10^{-25}\,\mathrm{cm}^2$). ζ_{i} and η_{i} are the collisional-ionization cooling and recombination cooling coefficient, respectively. $\omega_{\mathrm{He\,II}}$ is the dielectronic recombination cooling coefficient due to He II. ψ_{i} is the collisional excitation cooling coefficient and θ_{ff} the free–free cooling coefficient. Cooling due to Hubble expansion is accounted for by the term, $\frac{\dot{a}}{a}(\frac{kT_{\mathrm{e}}n_{\mathrm{B}}}{\mu})$ where $\frac{\dot{a}}{a} \equiv H$ is the Hubble constant. The factor of f_{Heat} is the amount of heat deposited by secondary electrons and is given by

$$f_{\mathrm{Heat}} = \begin{cases} 0.9971\left[1 - \left(1 - x_{\mathrm{ion}}^{0.2663}\right)^{1.3163}\right] & \text{if } x_{\mathrm{ion}} > 10^{-4} \\ 0.15 & \text{if } x_{\mathrm{ion}} \leqslant 10^{-4} \end{cases}.$$

The above expression is an extrapolation of fitting formula used in Shull & van Steenberg (1985) and the results of their calculations as plotted in their fig. 3. We here use the fact that the heating fraction never really goes to zero but saturates around a value of 0.15. The fitting formulas used in Shull & van Steenberg (1985) are appropriate for relatively HEs (typically >100 eV):

$$f_{\mathrm{H}}(x_{\mathrm{ion}}, E) = 0.3908\left[1 - x_{\mathrm{ion}}^{0.4092a(x_{\mathrm{ion}},E)}\right]^{1.7592}, \tag{13}$$

where $a(x_{\rm ion}, E)$ is

$$a(x_{\rm ion}, E) = \frac{2}{\pi} \arctan\left[\left(\frac{E}{0.12\,{\rm KeV}}\right)\left(\frac{0.03}{x_{\rm ion}^{1.5}} + 1\right)^{0.25}\right]. \qquad (14)$$

Note that the inclusion of an energy-dependent fitting formula for the fraction of energy that goes to ionization, as in equation (13) (Dijkstra, Haiman & Loeb 2004), does not alter the result significantly. This is due to the fact that the lower energy photons are trapped close to the vicinity of source for ionization and the remaining photons are of relatively HEs for which the fitting formula of Shull & van Steenberg (1985) holds.

The integrals in equations (1)–(12) are pre-calculated and tabulated as a function of n_i x_i, where the index 'i' refers to H I, He I or He II. n_i refers to the abundances and x_i is the ionized fraction of the ith species. In other words, we are tabulating the integrals as a function of optical depth per unit distance. Therefore, in principle, we should have a three-dimensional table, as is commonly used (Iliev et al. 2006). But the integration table in our implementation is at most two-dimensional. We get around using three-dimensional tables by utilizing the fact that the functional form for the photoionization cross-sections of HI and HeII are the same expect for a constant difference (see equations B13 and B16 of Fukugita & Kawasaki 1994).

2.2 The algorithm

The aim of the radiative transport code developed is to compute the fraction of the ionization for the species of hydrogen and helium and the temperature for points along a radial direction away from the source, at various times. This was achieved by solving the time-dependent rate equations (equations 1–12) using the ODEINT routine of Numerical Recipes (Press et al. 1992), using the implicit scheme of integration for *stiff* equations. The entire code was developed in ANSI C.

Fig. 1 shows the basic steps involved in the solution of these rate equations. First, the direction radial to the source is girded into cells, the sizes of which are decided as described later. The inputs to the code at this stage are the parameter space we desire to probe in this study which includes the spectrum, masses of the sources and the redshifts at which these sources switch on. The spectrum of the sources, broadly speaking is classified into power law and blackbody. The slopes of the power law and the temperature of the blackbody can be set to any desired value. Once the spectrum of the source is known, a lookup table for the values of the integrals appearing in the rate equation is created.

Before the start of the simulation, the initial conditions are setup as follows. The region around the source is set to be completely neutral with the primordial abundance fraction of hydrogen and helium. All species therefore have densities corresponding to that of the IGM at that epoch, $n_{\rm H}(z) = n_{\rm H}(0)(1+z)^3$, $n_{\rm He}(z) = n_{\rm He}(0)(1+z)^3$, where $n_{\rm H}(0) = 1.9 \times 10^{-7}\,{\rm cm}^{-3}$ and $n_{\rm He}(0) = 1.5 \times 10^{-8}\,{\rm cm}^{-3}$ are the IGM densities at a redshift zero of hydrogen and helium, respectively, or the initial density profile could also be set according to a profile as in equation (21). Abundances of all singly and doubly ionized species $n_{\rm HII}$, $n_{\rm HeII}$, $n_{\rm HeIII}$ and electron density $n_{\rm e}$ are set to zero. Initial kinetic temperature $T_{\rm e} = T_{\rm CMB}(z)(1+z)^2/(1+250)$. Here, we have assumed that the kinetic temperature of the gas was coupled to the cosmic microwave background (CMB) temperature ($T_{\rm CMB}$) till a redshift of 250, after which the $T_{\rm CMB}$ continued to fall off as $1/(1+z)$ and $T_{\rm e}$ like $1/(1+z)^2$.
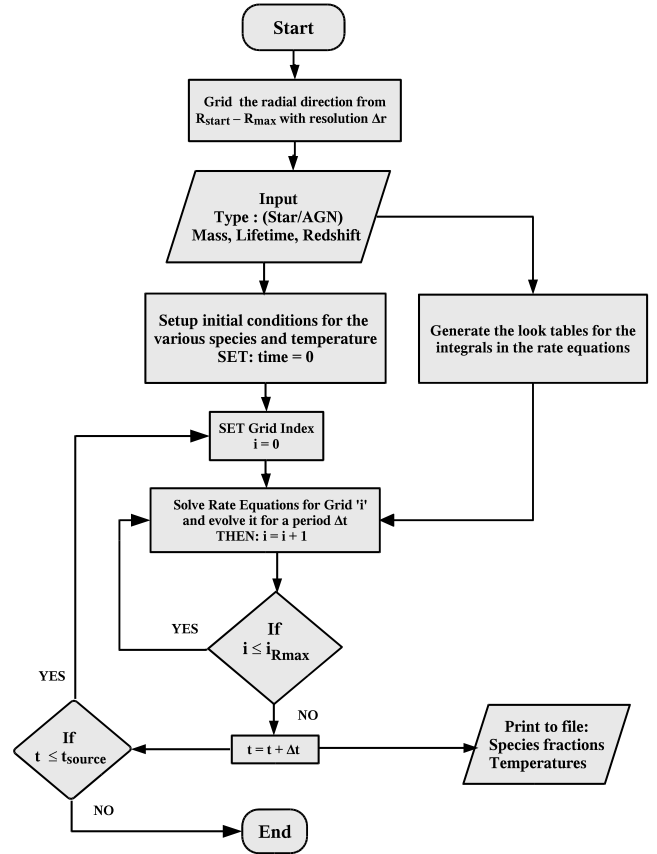

Figure 1. Flowchart outlining the basic modules in the algorithm implementing the RT code.

We start our simulation at $R_{\rm start}$, typically 0.1 physical kpc from the location of the source. All hydrogen and helium are assumed to be completely ionized inside this radius $R_{\rm start}$. The outcome of the calculations for different choices of $R_{\rm start}$ has been tested and, for the choice made in this paper, found to converge to the required accuracy.

Each cell is then updated for time Δt, which again is chosen based on a convergence criterion. This Δt is not the intrinsic time-step used to solve the differential equation itself because that is adaptive in nature and varies according to the tolerance limit set in the ordinary differential equation solver. On the other hand, the Δt here decides for how long a particular cell should evolve before moving on to the next. For example, we cannot evolve the first cell for the entire lifetime of the source and move on to the next cell. Therefore, Δt is decided by reducing it by half each time until two consecutive runs with Δt and $\Delta t/2$ give the same final result for the ionized sphere within a tolerance limit. As eluded to before, the code is causal in the sense that a cell $i + 1$ is updated after cell i. Note that the light travel time is not taken into consideration explicitly since the ionization front (I-front) is very subluminal. Hence, all cells are updated for time $n\Delta t$ at the nth time-step.

After all cells until the last cell $i_{\rm Rmax}$ are updated for time Δt, the resulting values are stored and then passed on as initial conditions for the evolution of the cell in the next Δt interval of time. The update of all $n_{\rm cell}$ is repeated n times such that $n\Delta t = t_{\rm quasar}$, where $t_{\rm quasar}$ is the lifetime of the miniquasar. The various quantities of interests can be stored in a file at intervals of choice.

A radial coverage of $R_{\rm max}$ is chosen a priori which, depending on the problem, can be set to any value. Typically, we do not need

to go above 10 comoving Mpc. This radius is then gridded equally with a resolution of Δr, which, like the time resolution, is decreased to half its value until it meets a given convergence criterion, which here is that the final position of the I-front is accurate within 0.5 per cent. For a typical run, which normally takes about 100 time-steps, this criterion gives an accuracy of about 5×10^{-5} per time-step.

The block computing the solution of the rate equations in Fig. 1 requires further explanation. Once the spatial resolution is set by following the procedure described above, we compute for every cell, $\sum_{1}^{j-1}(n_i x_i)_s$, where j is the grid-cell under consideration, and these computed sums are used to evaluate the values of the integrals in equations (1)–(12) from pre-computed tables through a simple polynomial interpolation. The initial conditions and the value of the integrals are passed to the solver ODEINT (Press et al. 1992) with the *driver* to solve the *stiff* equations. At the end of this run, all cells are updated for a time Δt.

3 TESTING THE CODE

In order to examine the performance of the code, we carry out three tests. The first test is against the analytical form of the velocity of the I-front with constant background density and central source emitting a fixed number of photons, namely, the Strömgen sphere case. The second is to compute the I-front velocity around a source again with a constant photon flux but with the background density evolving with redshift. This is then compared with the analytical solution of Shapiro & Giroux (1987). In both these cases, the I-front is defined as the position at which the ionized and neutral hydrogen fractions are equal. The third test was a comparison between an analytical model of heating (Zaroubi et al. 2007) and the RT code. The results agree well except in the discrepancy are discussed in the Appendix.

3.1 Test I: I-front velocity in simple cosmology

The first problem was to test the expanding H II bubble around a source that produces a fixed number of photons per unit time. Analytically, the position r_I and velocity v_I of the I-front can be written as

$$r_I = r_s[1 - \exp(-t/t_{rec})]^{1/3}, \tag{15}$$

$$v_I = \frac{r_s}{3t_{rec}} \frac{\exp(-t/t_{rec})}{[1 - \exp(-t/t_{rec})]^{2/3}}, \tag{16}$$

where r_s is the Strömgen radius (Dopita & Sutherland 2003), $r_s = \left[\frac{3\dot{N}_\gamma}{4\pi\alpha_B(T)Cn_H^2}\right]^{1/3}$, $t_{rec} = [C\alpha_B(T)n_H]^{-1}$ is the recombination time-scale, n_H is the neutral hydrogen density, C is the clumping factor and $\alpha_B(T) = 2.6 \times 10^{-13}(T/10^4)^{-0.85}$ cm^3 s^{-1} is the hydrogen recombination coefficient at temperature T. The parameters used for this example are: $\dot{N}_\gamma = 10^{54}$ S^{-1}, $C = 1$, $\alpha_B = 2.6 \times 10^{-13}$ cm^3 s^{-1} and $n_H = 1.87 \times 10^{-4}$ cm^{-3}.

The solid line in Fig. 2 is plotted based on equation (16) and the dashed line represents the numerical solution to the problem. The numerical solution obtained by the RD code is within 0.1 per cent of the theoretical value.

3.2 Test II: The Shapiro & Giroux test: ionization front in an expanding Universe

Shapiro & Giroux (1987) derived an analytical solution for the position of the I-front as a function of cosmic time in an expanding Universe that contains only hydrogen. The solution is of
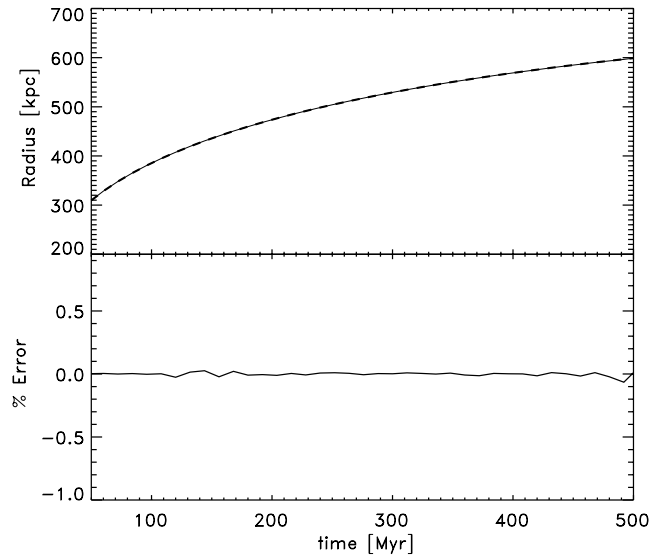

Figure 2. Top panel shows the simulated (solid) and the theoretical (dashed) results of the evolving I-front in an uniform background. These simulations include only hydrogen of constant density (i.e. no expansion).

the form,

$$y(t) = \lambda e^{\lambda t_i/t}[t/t_i E_2(\lambda t_i/t) - E_2(\lambda)], \tag{17}$$

where $y(t) \equiv [r_I(t)/r_{s,i}]^3$, t_i is the age of the Universe at the time the source has turned on and r_I and $r_{s,i}$ are the comoving I-front position radially from the centre of the source and the initial Strömgen radius $[3\dot{N}_\gamma/C\alpha_B(T)n_H^2]^{1/3}$, respectively. Here, n_H is the comoving density of hydrogen at source turn-on time. $\lambda \equiv t_i C\alpha_B(T)n_H$ is basically the ratio between cosmic source turn-on time and the recombination time-scale. $E_2(x)$ is an exponential integral of the form $E_2(x) = \int_1^\infty e^{-xt}/t^2 \, dt$.

Result of the test is plotted in Fig. 3. The numerical and analytical solutions here also agree to within a couple of tenth of a per cent throughout the evolution of the I-front.
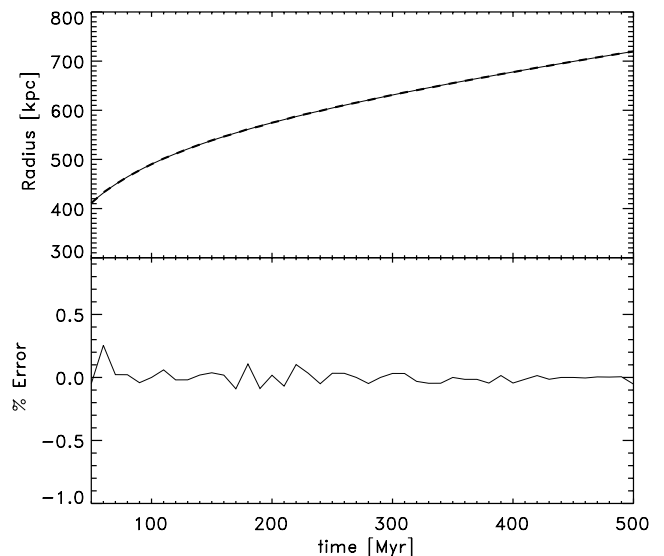

Figure 3. Top panel shows the simulated (solid) and the theoretical (dashed) results of the evolving I-front in an expanding Universe with background density being that of the IGM at that epoch.

4 APPLICATION TO POWER-LAW SOURCES (MINIQSOS)

Sources of ionizing radiation with a power-law spectral energy distribution have been considered by many authors (e.g. Fukugita & Kawasaki 1994; Madau et al. 1997; Kuhlen & Madau 2005; Nusser 2005; Zaroubi & Silk 2005; Zaroubi et al. 2007). The radiative transport code is applied to these power-law sources where the ionization and heating patterns around them are studied as a function of their spectral index, mass and redshifts. For some of the plots in this section, we have assumed masses of quasars of the order of $10^6 \, M_\odot$. Although recent works like Volonteri, Lodato & Natarajan (2008) does show that there could be relatively massive black holes at early redshifts, a $10^6 \, M_\odot$ would be unlikely. But we have included this case in our discussion for a completeness in spanning the parameter space and also to clearly distinguish the various effects of these sources on the IGM. In the following sections, we introduce and discuss our main findings.

4.1 Energy spectrum of miniquasars

Recent observations and catalogues published in the literature (Elvis et al. 1994; Laor et al. 1997; Vanden Berk et al. 2001; Vignali, Brandt & Schneider 2003) suggest that the energy spectrum of quasars follows a power law of the form $E^{-\alpha}$. Specifically, we explore two types of power-law spectra:

$$I(E) \propto E^{-\alpha} \begin{cases} \text{if} & 10.4\,\text{eV} < E < 1\,\text{keV (LE case);} \\ \text{if} & 200\,\text{eV} < E < 1\,\text{keV (HE case).} \end{cases}$$

The value of α is fixed to unity for most of the study, although in Section 4.4, we do briefly discuss the effects of varying this parameter. LE and HE stand for the 'Low Energy' and the 'High Energy' lower limits to which the spectral energy distribution extents. The HE case is considered in order to take into account, in an approximate manner, the possibility of the lower energy photons being absorbed in the close vicinity of the source. Instead of single slope one can also adopt multislope spectral templates (Sazonov, Ostriker & Sunyaev 2004) but this is not done in this study.

The miniquasars are assumed to accrete at a constant fraction ϵ (normally 10 per cent) of the Eddington rate. Therefore, the miniqso luminosity is given by

$$L = \epsilon \, L_{\text{edd}}(M) \tag{18}$$

$$= 1.38 \times 10^{37} \left(\frac{\epsilon}{0.1} \right) \left(\frac{M}{M_\odot} \right) \text{erg s}^{-1}. \tag{19}$$

The luminosity derived from the equation above is used to normalize the relation in 18 according to equation (8). The normalization, both for the HE and LE case, is done for an energy range of 10.4 eV to 1 keV. Simulations were carried out for a range of masses between 10 and $10^6 \, M_\odot$. Although the number of photons at different energies is a function of the total luminosity and spectral index, if we assume that all photons are at the hydrogen ionization threshold, then the number of ionizing photons thus obtained for the mass range given above is of the order of 10^{50}–10^{55}. These are of the same order of magnitude of the number of ionizing photons being employed for simulations by various authors, Mellema et al. (2006) and Kuhlen & Madau (2005), for example.

4.2 Radial profile of species' fraction

Plotted in Figs 4 and 5 are snapshots of the neutral fraction as a function of the radial distance away from the centre of the black
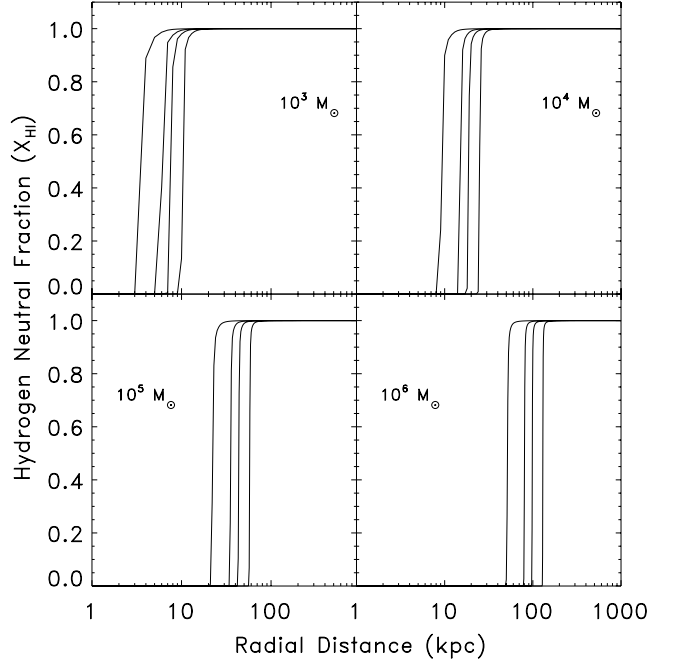

Figure 4. The neutral hydrogen fraction as a function of distance from the centre of the black hole with masses $10^{3,4,5,6} \, M_\odot$ (top left-hand panel to bottom right-hand panel) at redshift $z = 20$ is shown. Four lines in each panel indicate the position of the I-front after 1, 3, 5 and 10 Myr. These are miniquasars with no UV ionization photons. ($200 < E < 10^4$ eV).
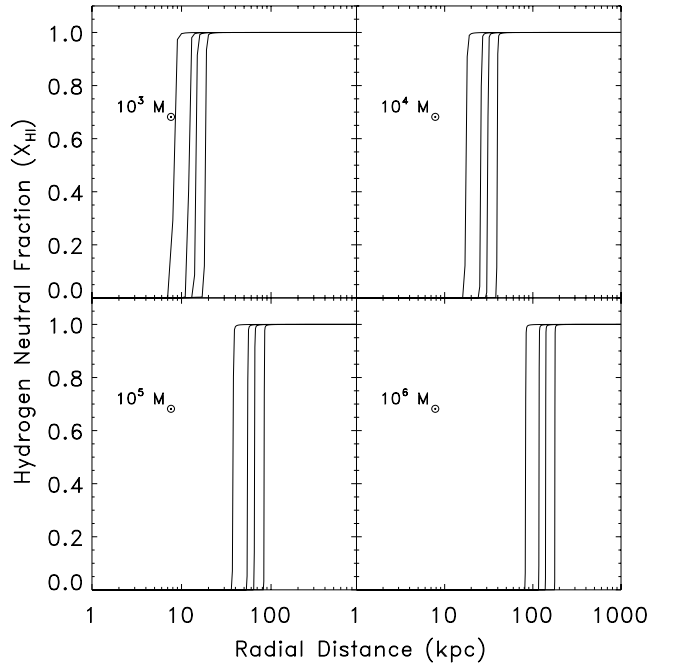

Figure 5. Same as in Fig. 4 but now including UV ionizing photons ($10.4 < E < 10^4$ eV).

hole for two different cases. The first (Fig. 4) is the HE case, i.e. without LE photons. Whereas, the second (Fig. 5) is for the LE case, i.e. the photon energy range spans 10.4 to 10^4 eV. As indicated on the figure, each panel corresponds to a different mass. The lines in each panel correspond to snapshots of the neutral fraction at 1, 3, 5

and 10 Myr. In the both cases, the sources are turned on at a redshift of 20.

Fig. 5 clearly shows that the size of the ionized regions is substantially larger than those in Fig. 4. Even the 1000 solar mass miniqso produce regions that are tens of kpc in physical size. This is due to the increase in the number of photons in the LE range (13.6–200 eV), which increases the probability of a photon – atom interaction relative to the HE case ($\sigma \propto E^{-3}$). Equilibrium is only reached when the miniquasar lifetime approaches the recombination time-scale. Since the problem is set in an expanding Universe we never actually reach an equilibrium solution (Shapiro & Giroux 1987). We see that the ionized bubble gets to a couple of hundred kpc for the case of HE photons and to more than 0.5 Mpc for 10^6 $M_\odot$ miniqsos with LE photons. All distances plotted in the figures are physical unless specified otherwise.

The abundance of H I, H II, He I, He II and He III as a function of radial distance is tracked in time. Figs 6 and 7 show the fraction of these species after 10 Myr of evolution as a function of radius. The miniquasar is switched on at a redshift of 20.

The interplay between the evolution of these species among each other and with the gas temperature provides us with rich and in-
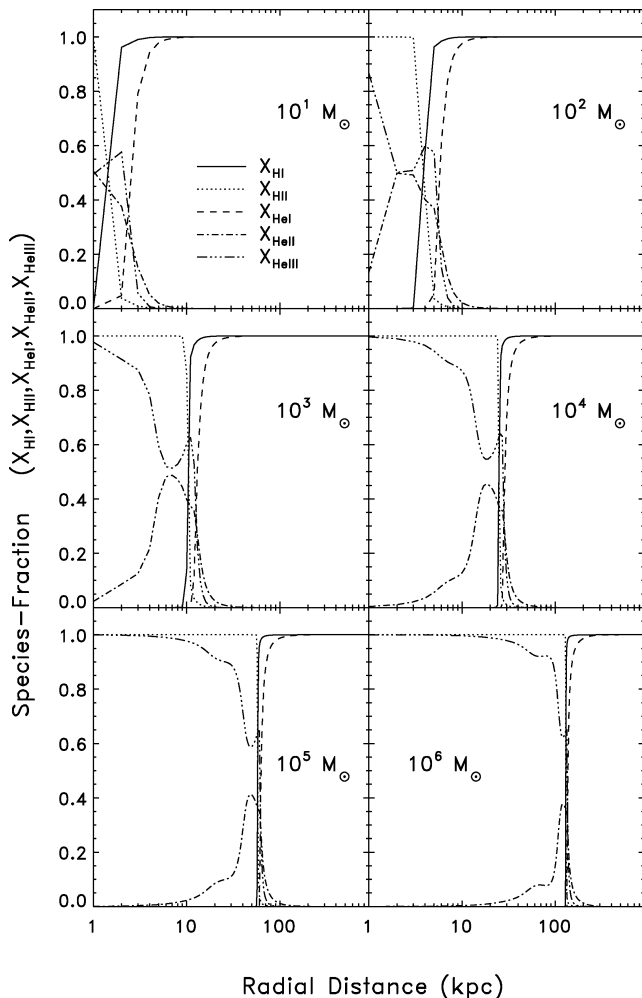
Figure 7. Same as in Fig. 6 but now including UV ionizing photons ($10.4 < E < 10^4$ eV).

teresting structures in profiles. Miniquasars of 10 and 100 solar masses are not able to produce substantially high number of ionizing photons, and hence the ionized regions around them are relatively small. However, miniquasars of higher masses like 10^5 and 10^6 solar masses produce ionized bubbles of a couple of comoving Mpc.

An interesting detail apparent in these figures is that the He I I-front exceeds that of the H I. Explanation for this lies in the fact that we have relatively HE photons ($E > 50$ eV) and the cross-section of H I is much smaller than He I, $\sigma_{He I}(E)/\sigma_{H I}(E) \approx 20$ at an energy $E = 50$ eV. Therefore, the probability of HE photons being capture by He I is higher, increasing the helium I-front distance from the centre.

Results are shown for the HE (6) and LE (7) cases. As expected, the ionized fronts of H I and He I have travelled a much greater distance in the LE case. This is consistent because the HE spectrum is not only devoid of hydrogen ionizing photons but also lacks helium ionizing photons (54.4 eV).

Another point to note is the visible excess of H I fraction in the HE spectrum just before the full ionization front in Fig. 4, especially at the 10 Myrs curves. We interpret this excess as a result of the interplay between the increase in He II and decrease in He III as seen in Fig. 6, thus increasing the H I recombination rate on the one hand and decreasing photon flux as a function of radius on the other. This interpretation is supported by the weakening of the H I excess feature

Figure 6. Fraction of various species ($x_{HI}, x_{HII}, x_{HeI}, x_{HeII}, x_{HeIII}$) as function of distance from the centre of the black hole with masses $10^{1,2,\ldots 6}$ $M_\odot$ (top left-hand panel to bottom right-hand panel) at redshift $z = 20$. These are snapshots after 10 Myr of evolution. Miniquasars have no UV ionization energy ($200 < E < 10^4$ eV).
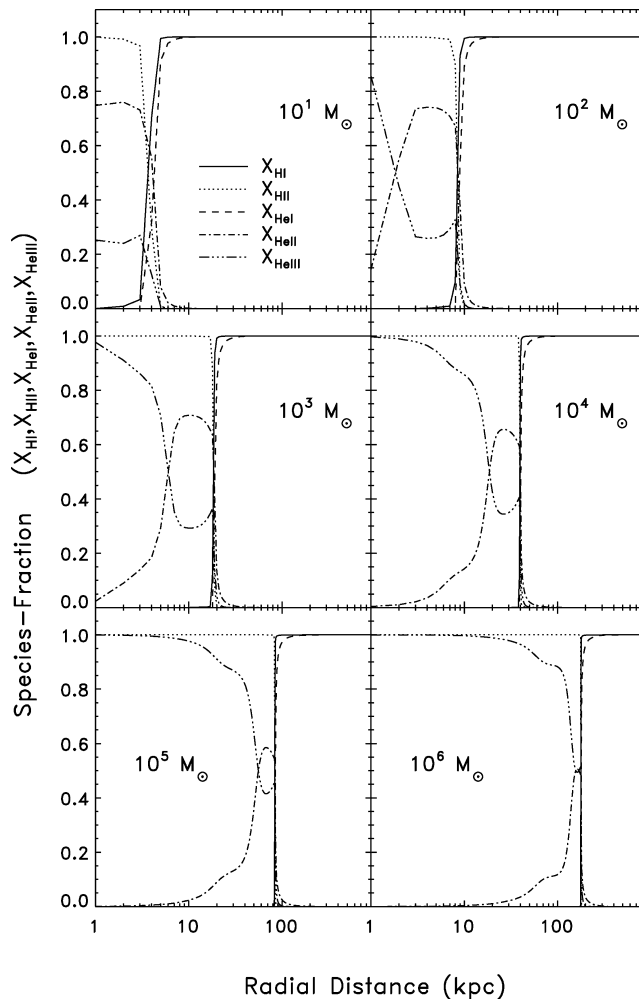
as a function of black hole mass. The phenomena are not manifested in the LE spectrum (Fig. 5) due to the ionization efficiency of the UV photons.

4.3 The kinetic temperature profile

The heating and cooling terms included in equation (12) are coupled with the rate equations (1)–(3). The principal heating terms are the bound–free and Compton heating. Bound–free heating is by far the most dominant, although towards the centre Compton heating does become important.

Figs 8 and 9, corresponding to the HE and LE cases, respectively, show the temperature profile for masses from 10 to 10^6 $M_\odot$ for four different redshifts. The snapshot is taken after 3 Myr of evolution.

Although there is a substantial change in the ionization profiles (sizes of the ionized spheres), the heating remains more or less the same except for a few details. The flux of HE photons, those responsible for the dominant secondary heating is abundant causing a sort of invariance in the extent of heating in the both cases. Miniqsos of high masses do maintain an extended volume of high temperatures, in some cases up to five comoving Mpc. If this indeed is the case at
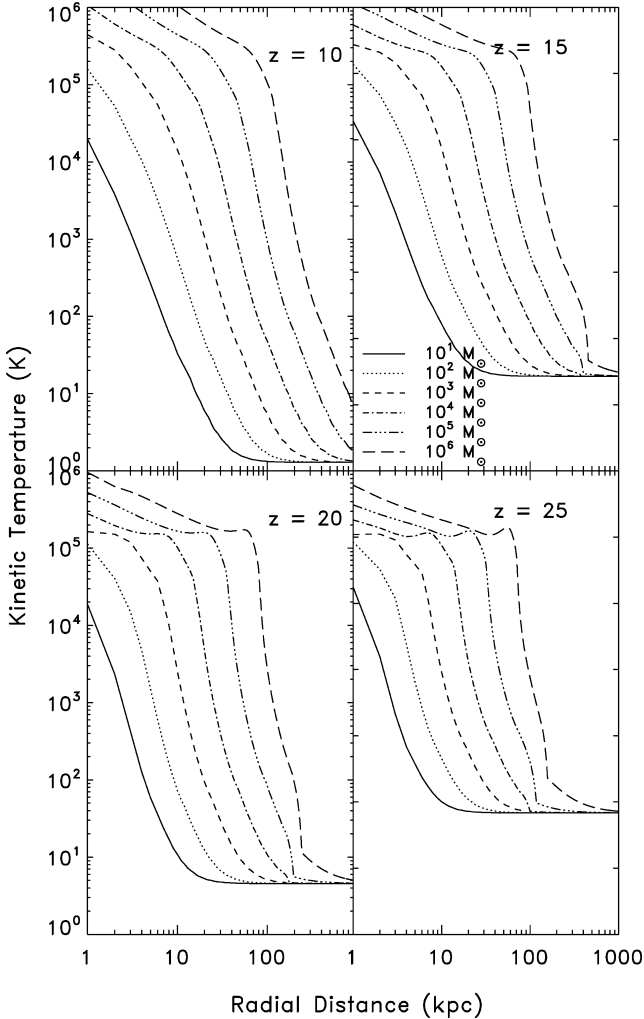
Figure 8. Radial profile of Kinetic temperature T_e for black hole with masses $10^{1,2,...6}$ $M_\odot$ at four different redshift $z = 10, 15, 20, 25$ (top left-hand panel to bottom right-hand panel) after 3 Myr is shown. The spectrum of these quasars includes only HEs.
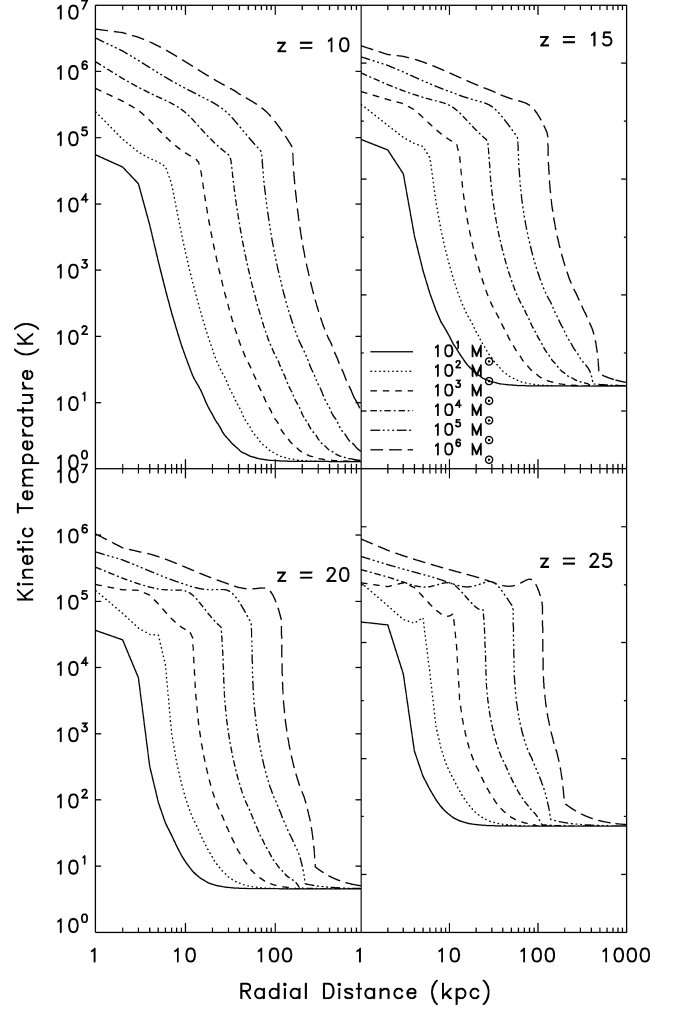

Figure 9. Same as in Fig. 8 but these quasars do include the LE photon.

relatively low redshifts like around six, then they will be observable in the SZ effect as discussed in Section 7.

The four panels corresponding to different redshifts do not show a significant difference in the heating or its extent. Whereas the ionized bubbles (Figs 4 and/or 5) are strongly dependent on the redshift. This is due to the fact that lower energy photons (responsible for ionizing) see a much higher optical depth in neutral hydrogen than do HE photons. Thus, an increase in density by an order of magnitude (from $z = 10$–25) does not alter the heating considerably.

4.4 Influence of different spectral energy distributions

Throughout our study in this paper, we have dealt with $\alpha = 1$ case for equation (18). Here, we explore the possibility of other indices for the power law. As an example, we plot (Fig. 10) the size of the ionized bubbles after 10 Myr as a function of α around a quasar with central black hole of 10^5 $M_\odot$ for four different redshifts as indicated in the figure. Fig. 10 shows that the size of the ionized bubble[5] increases with α. This is expected because an increase in

---

[5] We define the size of the ionized bubble as the position of the I-front when the ionized fraction is 0.5 for hydrogen.
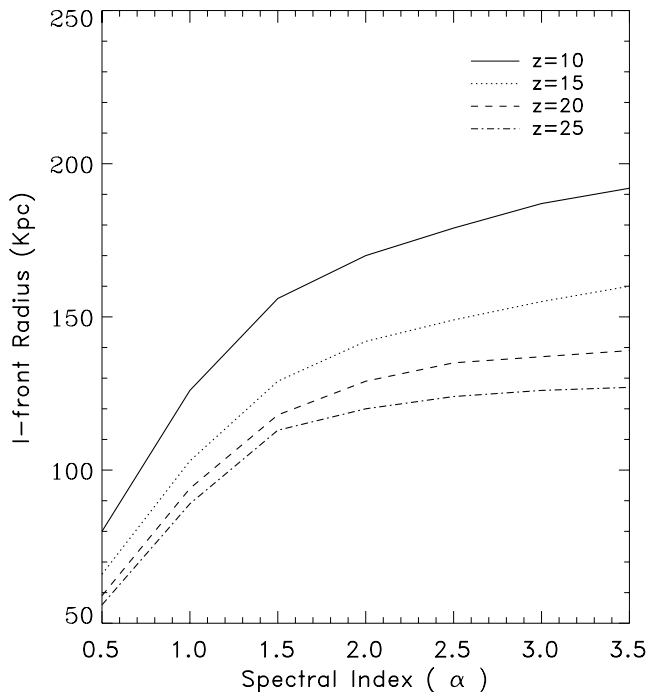
Figure 10. Position of the I-front is plotted in physical size as a function of spectral index α, 10 Myr after the quasar was switched on. Note that the sizes of the ionized region plateaus after about $\alpha = 2.5$. The black hole in the centre is of $10^5\,M_\odot$.

Figure 11. Temperature around a $10^5\,M_\odot$ black hole is plotted for three different spectral indices at $z = 20$. We see the decrease in heating with steeper indices. Decrease in LE photons being the cause of this behaviour.

Figure 12. Figure shows the neutral fraction (top panel) and kinetic temperature (bottom panel) for three different times after the quasar was switched on as indicated in the figure. The quasar is at redshift $z = 10$ and hosts a $1000\,M_\odot$ black hole in the centre, which is switched on for the first 10 Myr and switched off since then.

α for the same given normalization concentrates more photons at the LE end, i.e. around 13.6 eV and fewer HE photons. Thus, for higher α, one expects more ionization and less heating. This indeed is reflected in Fig. 11.

The central regions are heated more or less to the same extent. In order to see the significant difference, we have only plotted the distances between 100 and 1000 kpc physical. It is clearly seen that for steeper slope heating drops considerably.

4.5 Lifetime and duty cycle of mini-quasars

Wyithe & Loeb (2002) produce analytical estimates of the quasar lifetime and duty cycle (see their fig. 3). Certainly this sort of periodic switching on and off of the quasar leaves an imprint on the IGM. We simulate a case wherein the quasar duty cycle is 100 Myr with an active phase of 10 Myr at the start of the cycle.

Recombination time-scales are orders of magnitude larger than the ionization time-scales at the mean densities of the IGM. As a result, once the IGM is ionized by a source with finite lifetime (say 10 Myr), it takes considerably long time for the IGM to recombine, leaving behind a bubble of ionized gas. Fig. 12 shows the ionized fraction and the temperature profile just after the source is switched off at 10 Myr, than at 50 Myr and at the end of the duty cycle which is 100 Myr. The source is a miniqso of a $1000\,M_\odot$ at a redshift of 20.

There are a couple of points to be noted here. One is the fact that the I-front position is further away at 50 and 100 Myr than at 10 Myr although the source was switched off after 10 Myr. This propagation of the I-front in the absence of photons from the source is attributed to the ionization due to collisions. This continues until the temperature drops sufficiently so that collisions become
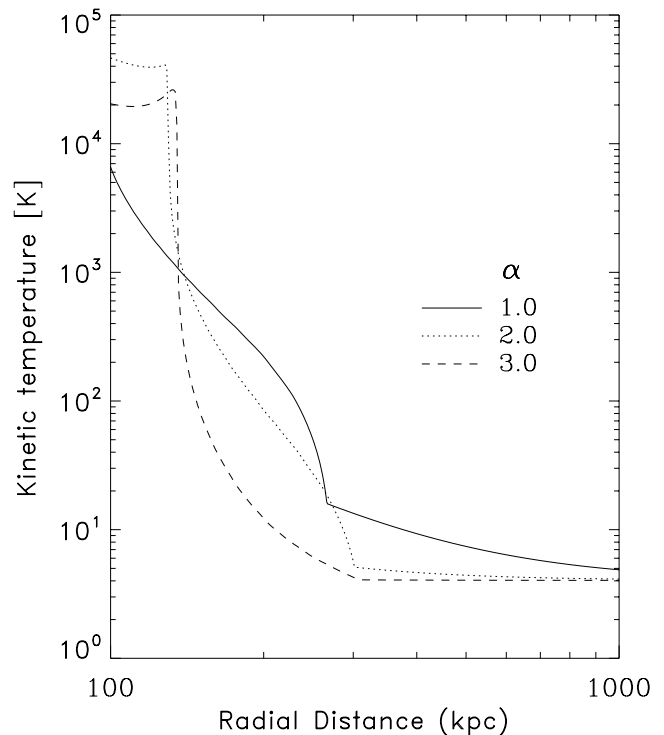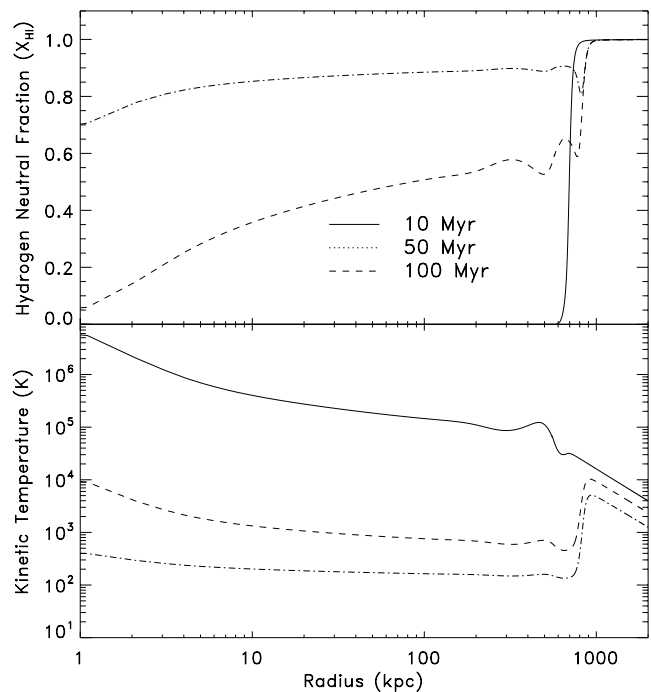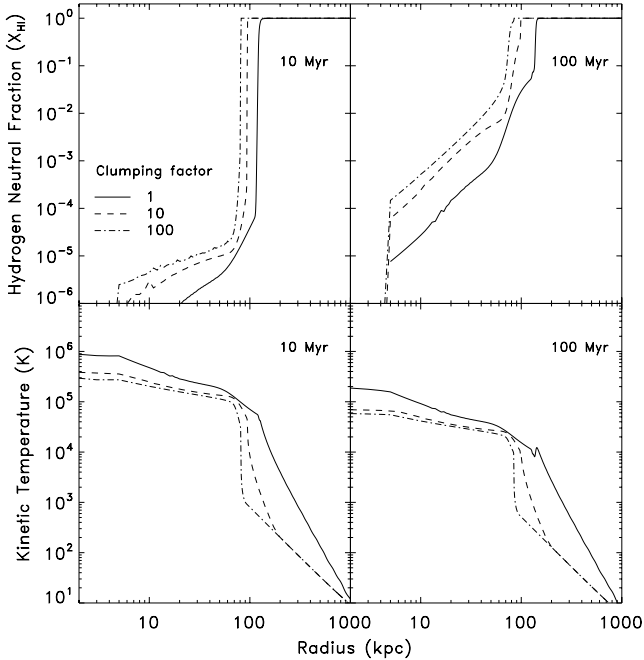
Figure 13. Figure shows the neutral fraction (top panels) and kinetic temperature (bottom panels) for three different clumping factors of 10 and 100 Myr as indicated. The quasar is active at redshift $z = 20$ and hosts a 1000 $M_\odot$ black hole in the centre, which is switched on for the first 10 Myr and switched off since then.

ineffective. In fact before the IGM recombines completely, the quasar is switched on again. Thus, we see[6] that the ionizing front expands during the on time, stands still around the same position during the off-time and continues to expand during the next on time and so on.

The drop in temperature on the other hand is easily seen within this turn-off period. Compton cooling is the dominant sink for the temperature. Also we see that the regions close to the centre remain relatively more ionized than the rest. This is again a consequence of the temperature profile. Regions with higher temperature continue to be ionized for longer periods.

All of the analysis performed thus far was done by embedding the source in a uniform background. But we know that objects like quasars are preferentially formed in overdense regions. In order to test the impact of different overdensities on the I-front position and temperature produced by a quasar, we embedded the quasar in a background, i.e. 1, 10 and 100 times the mean IGM density. The results are shown in Fig. 13. The miniqso has a 1000 $M_\odot$ black hole at the centre, and is at a redshift of 10 and contains only the HE photons. As expected the ionization fronts could penetrate less at higher densities. But the recombination rate is much greater at higher densities. This is seen in the top right-hand panel corresponding to 100 Myr as the I-front corresponding to a clumping factor of 100 has recombined much more. On the other hand, the heating is relatively less at higher densities because most of the photons are absorbed to ionize and the dominant cooling terms, e.g. like the Hubble cooling, are enhanced at higher densities.

---

[6] Movies created from the simulation can be obtained by contacting the authors.

5 APPLICATION TO STELLAR (BLACKBODY) SOURCES

Unlike quasars and miniqsos that have a power-law distribution of energy in their spectrum, the stars approximately behave as a blackbody of a given temperature. This blackbody nature of the source leaves different signatures in the manner the IGM is heated and ionized. Given the weak dependence of the star's temperature on its mass (see Schaerer 2002), we fix the blackbody temperature of the stars to 5×10^4 K and mass ranges between 10 and 1000 $M_\odot$. The total luminosity for a given stellar mass is calculated from table 3 of Schaerer (2002). The other difference in case of stars is the density profile in which it is embedded. We assumed a density profile of the form

$$\rho(r) = 3.2 \times (91.5\,\mathrm{pc}/r)^2\ (\mathrm{cm}^{-3})\quad (r \leqslant r_c),$$
$$= n_i(0) \times (1+z)^2\ (\mathrm{cm}^{-3})\quad (r > r_c), \tag{20}$$

where $n_i(0)$ is the density of the hydrogen or helium at a redshift of zero and r_c is the radius at which the density profile falls to that of the mean IGM.

Depending on the temperature, the spectrum used above for the stars peaks in between ≈ 20 and ≈ 24 eV (for 10^5 K). What is expected in the case of stars of the same power output as a quasar are bigger ionized bubbles and less heating. Simply because, after the peak, which is around the ionization threshold of hydrogen and helium, we have an exponential cut-off towards higher frequencies.

After modifying the spectrum and the underlying density profile, we basically did the same exercise as for the miniqsos. Some of the results are plotted in the following figures. The hydrogen neutral fraction is plotted in Fig. 14 as a function of distance from the source with an effective blackbody temperature of 50 000 K. Note that unlike the miniqsos case, the x-axis here runs only up to 100 kpc
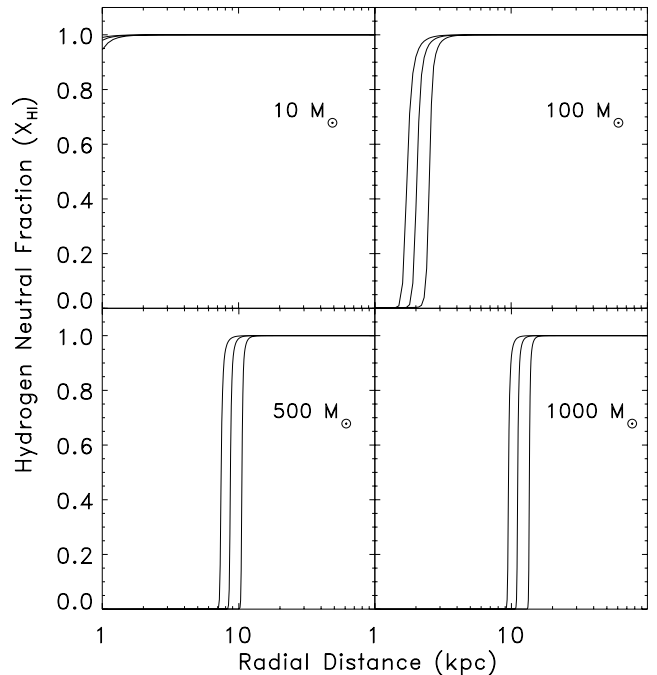

Figure 14. The neutral hydrogen fraction as a function of distance from the centre of the blackbody with an effective temperature of 50 000 K and masses 10, 100, 500, 1000 $M_\odot$ (top left-hand panel to bottom right-hand panel) at redshift $z = 20$. The three lines correspond to the I-front position after 2, 3 and 5 Myr of evolution.
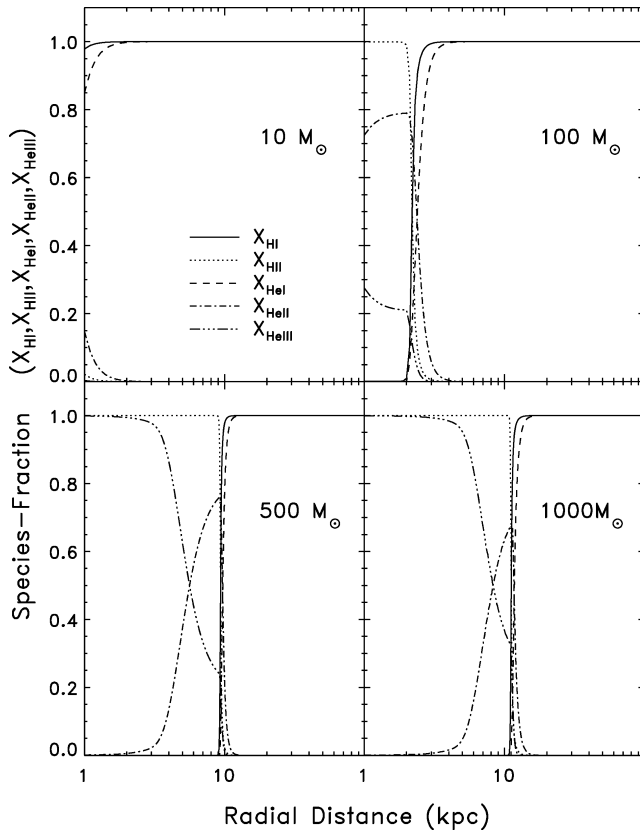
Figure 15. Fraction of various species ($x_{\mathrm{H\,I}}, x_{\mathrm{H\,II}}, x_{\mathrm{He\,I}}, x_{\mathrm{He\,II}}, x_{\mathrm{He\,III}}$) for the shown star masses.

physical. This is because the most massive stars considered here, i.e. $1000\,\mathrm{M_\odot}$, have a luminosity of a $10\,\mathrm{M_\odot}$ black hole shining at the Eddington rate (Schaerer 2002).

A similar case of lower ionized helium is seen in Fig. 15. Observe again that the helium front is leading. Because for high-temperature stars, the blackbody peaks at higher energies closer to the ionization threshold of helium.

Fig. 16 shows kinetic temperature as a function of radial distance for Pop III stars with masses of 10–$1000\,\mathrm{M_\odot}$. Note that even though the maximum temperatures reached are comparable to that of the miniqso, the extent and the shape of the profile are distinctly different. There is a much sharper edge to the heating attributed to the fact the there are not many HE (100 eV and above) photons, and hence the mean free path of most photons is lower.

6 OBSERVATIONAL EFFECTS

There are many indications of an EoR in the Universe. But observations currently are only able to provide us with either an integral limit (CMB data) or a lower limit (Gunn–Peterson troughs) on the redshift of reionization. Direct detection and study of this epoch currently rests on the future 21-cm radio observations and temperature fluctuations because of the SZ effect (detectable by *Planck*[7]) and probable direct observations of very high redshift Pop III stars by JWST.[8]
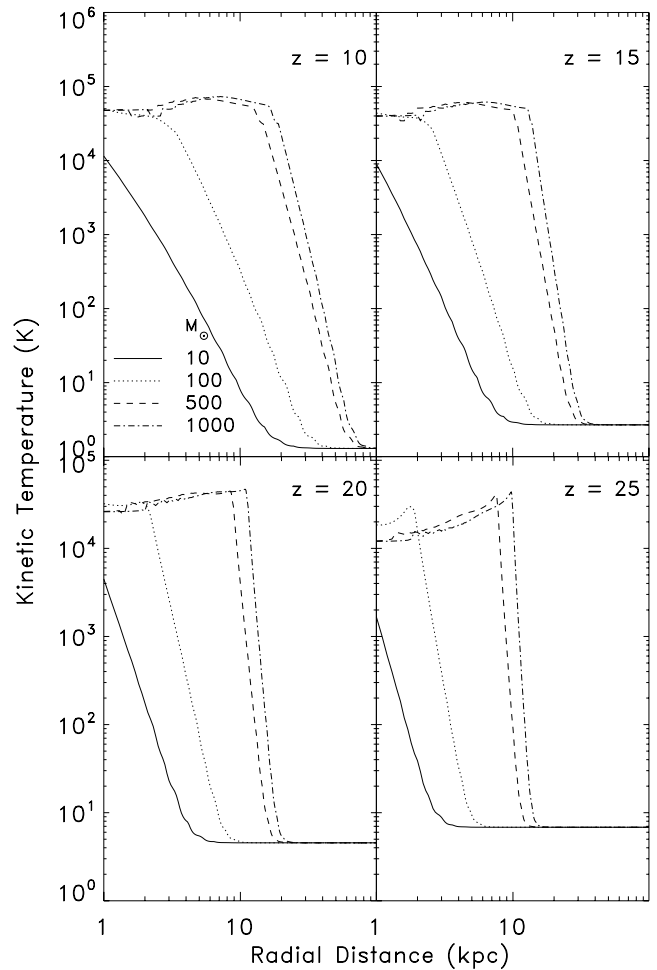
Figure 16. Radial profile of Kinetic temperature T_e for stars with masses 10, 100, 500 and $1000\,\mathrm{M_\odot}$ at four different redshift $z = 10$, 15, 20 and 25 (top left-hand panel to bottom right-hand panel) is shown.

In this paper, we will concentrate on the feasibility of radio observations on the detection and mapping of the EoR. A point to note is that from here on in the case of miniqsos we only use the LE case because the heating would be less exaggerated and probably closer to reality.

6.1 Spin temperature

The spin temperature T_s couples to either the CMB temperature T_{CMB} or the kinetic temperature T_e, in the absence of other radio sources (Field 1958; Kuhlen, Madau & Montgomery 2006). Thus, T_s can be written as a weighted sum between T_e and T_{CMB}:

$$T_s = \frac{T_\star + T_{\mathrm{CMB}} + y_{\mathrm{col}}T_e + y_\alpha T_e}{1 + y_{\mathrm{col}} + y_\alpha}. \tag{21}$$

$T_\star = h\nu_{21\,\mathrm{cm}}/k = 0.0681\,\mathrm{K}$, y_{col} and y_α determine the efficiency of collisional and Lyα coupling and is given by

$$y_{\mathrm{col}} = \frac{T_\star}{A_{10}T_e}(C_{\mathrm{H}} + C_e + C_p), \tag{22}$$

where $A_{10} = 2.85 \times 10^{-15}\,\mathrm{s^{-1}}$ is the spontaneous emission rate or the Einstein A coefficient and C_{H}, C_e and C_p are the de-excitation rates of the triplet due to collisions with neutral atoms, electrons and protons, respectively. The empirical fits for these coefficients are identical

to those used by Kuhlen et al. (2006), which is a combination of results published in Zygelman (2005), Allison & Dalgarno (1969), Liszt (2001) and Smith (1966), and the Lyα coupling coefficient (discussed in Section 6.2):

$$y_\alpha = \frac{16\pi^2 T_\star e^2 f_{12} J_o}{27 A_{10} T_e m_e c}. \tag{23}$$

Here, J_o is the Lyα flux density. For the miniqsos HE photons, Lyα coupling is mainly caused by collisional excitation due to secondary electrons (Chuzhoy, Alvarez & Shapiro 2006). This process is accounted for by the following integral

$$J_o(r) = \frac{\phi_\alpha c}{4\pi H(z) v_\alpha} n_{\rm H1}(r) \int_{E_o}^\infty \sigma(E) N(E;r) \,{\rm d}E, \tag{24}$$

where $f_{12} = 0.416$ is the oscillator strength of the Lyα transition, e and m_e are the electron's charge and mass, respectively. ϕ_α is the fraction of the absorbed photon energy that goes into excitation (Shull & van Steenberg 1985). The contribution of this term is important close to the miniquasar.

Note that in reality, we have to include the frequency dependence of the Lyα cross-section, the background continuum Lyα photons and scattering (Chen & Miralda-Escude 2006). But since we are dealing only with 'injected' photons at the Lyα frequency, we only include the cross-section at the line centre with thermal broadening.

Results of the spin temperature for a black hole of mass $10^4\,{\rm M}_\odot$ are shown in Fig. 17 for four different redshifts. For reasons discussed in the next section, the spin temperature follows the kinetic
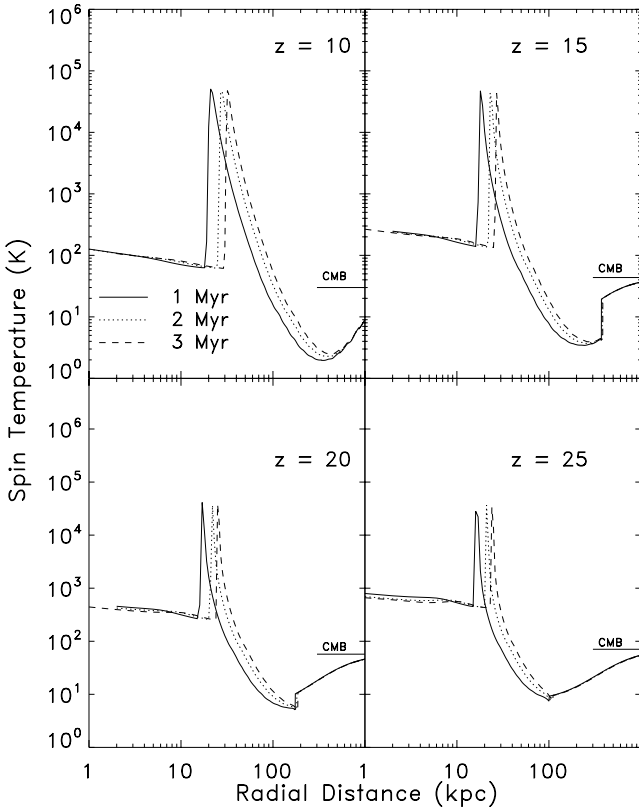
Figure 18. Radial profile of spin temperature T_s for stars with a mass $1000\,{\rm M}_\odot$ at four different redshifts $z = 10$, 15.0, 20 and 25 (top left-hand panel to bottom right-hand panel) is shown. The temperature of the star is assumed to be $50\,000\,{\rm K}$.

temperature for considerable distance away from the source and then follows the background CMB temperature at larger distances.

The spin temperature for the case of a $1000\,{\rm M}_\odot$ at four different redshifts is shown in Fig. 18. The spin temperature, for the case of stars, is assumed to follow the kinetic temperature for a distance of 'ct', although this might be an overestimate because there is a sharp cut-off towards redward of the black body peak reducing the number of Lyα produced by the source itself. But with a combination of the background Lyα, it might be possible to couple the spin temperature to the kinetic temperature.

6.2 Lyα coupling

Lyα coupling is known to be the most efficient mechanism to couple the kinetic temperature to the spin temperature, at least in the mean IGM. Collisional coupling only becomes important in overdense regions with gas overdensities $\delta \geqslant 20[(1+z)/10]^{-2}$ (Furlanetto & Loeb 2002; Iliev et al. 2003). Since we are interested in studying brightness temperature fluctuation relatively far away from the source, the dominant mode of coupling for our purposes is Lyα pumping.

There are a number of ways to generate Lyα photons. (i) The source itself produces continuum photons between Lyα and Lyβ, which is then redshifted at a distance from the source to Lyα. (ii) Photons above the Lyβ produced by the source pump the electrons to higher levels which then cascade back to produce Lyα. (iii) Secondary electrons can deposit a part of their energy towards

Figure 17. Radial profile of spin temperature T_s for a black hole with mass $10^4\,{\rm M}_\odot$ at four different redshift $z = 10$, 15, 20 and 25 (top left-hand panel to bottom right-hand panel) for 1, 2 and 3 Myr of evolution after the source was switched on. Note that the curves identical to that of the kinetic temperature in Fig. 9 except the spin temperature climbs back to $T_{\rm CMB}$ after about 1000 kpc corresponding to the photon propagation distance in 3 Myr. These miniquasars include the LE photons.
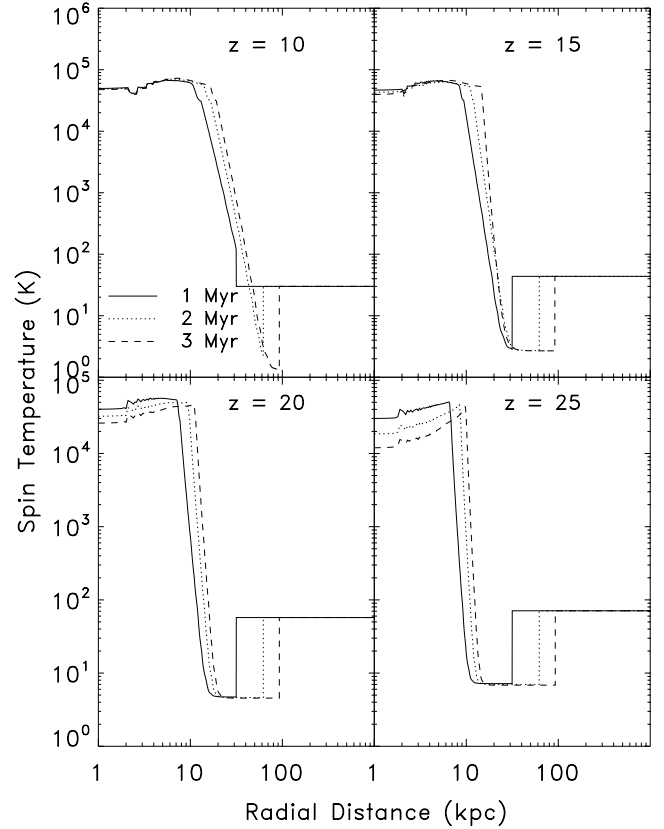
exciting the hydrogen atom (Shull & van Steenberg 1985). (iv) If we are looking at sources at lower redshifts (<20) then there is enough background Lyα from 'first stars' Ciardi & Madau (2003).

The Lyα flux density estimated in equation (25) is efficient to couple the spin temperature to the kinetic temperature. The Wouthuysen–Field effect[9] is efficient within the photon propagation (or light travel) time if these photons come directly from the source within the energy range of ionization (13.6 eV) and Lyα (10.4 eV). But, even in the case when the source does not produce Lyα photons, the secondary excitations are efficient enough to couple T_s with T_e to a large distance away from the source as seen from Fig. 17. But at lower redshifts, the background Lyα flux would be large enough to decouple T_s from T_{CMB} much further away from the source (Ciardi & Madau 2003). In the case of stars, we do not expect a major influence of the secondary electrons on ionizations or excitations. Thus, we assume that the Lyα flux originates from the source/background. Hence, we allow the spin temperature to follow the kinetic temperature to the light travel distance 'ct'.

6.3 Brightness temperature

Under the 'low frequency' or 'Rayleigh–Jeans' approximation, the equation for blackbody radiation reduces to

$$I(\nu) = \frac{2\nu^2}{c^2} k T_b, \tag{25}$$

where $I(\nu)$ is the intensity of radiation at frequency ν, k is the Boltzmann constant, c is the speed of light and T_b is the brightness temperature. In radio astronomy, this limit is applicable. Brightness temperature can be measured differentially as a deviation from the background CMB temperature T_{CMB} (Field 1958; Ciardi & Madau 2003) as

$$\delta T_b = 26\,\mathrm{mK}\,(1+\delta)\,x_{HI}\left(1 - \frac{T_{CMB}}{T_s}\right)\left(\frac{\Omega h^2}{0.02}\right)$$
$$\times\left[\left(\frac{1+z}{10}\right)\left(\frac{0.3}{\Omega_m}\right)\right]^{1/2}, \tag{26}$$

where x_{HI} is the neutral hydrogen fraction (see Fig. 4), δ is the overdensity of hydrogen (atoms and ions) and T_s is the spin temperature (Fig. 17). So given the cosmology and the redshift, which translates to a frequency of observation, the brightness temperature in equation (27) basically reflects the source characteristics in two ways. One that enters through the neutral fraction x_{HI}, defined by the ionizing capabilities of the source and another through the spin temperature T_s which in effect reflects kinetic temperature dictated by the heating capacity of the source. Thus, we hope that a three-dimensional tomography could not only reveal a statistical signal, the power spectrum and the large-scale structure of the epoch reionization but also give us clues on the nature of these first sources.

As an example, we can consider the HE and the LE case. Although the heating pattern and extent in both these cases are similar (see Figs 8 and 9), the ionization profiles are indeed different (see Figs 4 and 5). This according to equation (27) will be reflected in the brightness temperature.

Fig. 19 shows the radial profile for the expected brightness temperature for the same case as discussed in the context of the spin temperature above. For all the cases, there is almost a sudden jump
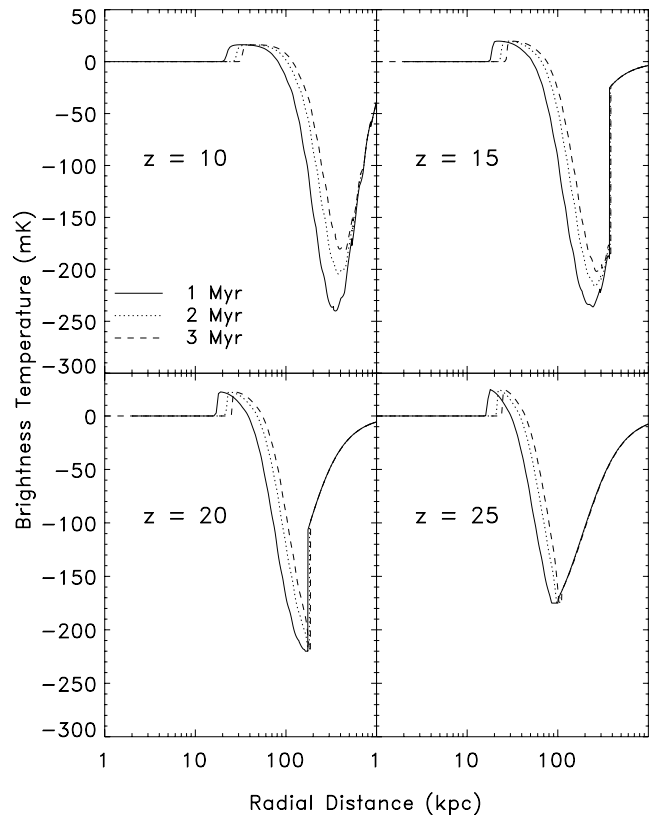
[9] The Wouthuysen–Field mechanism basically is the mixing of the hyperfine state in neutral hydrogen in its ground state via intermediate transitions to the 2p and above states (Wouthuysen 1952; Field 1958).

Figure 19. Radial profile of brightness temperature d*Tb* for the same black hole model as in Fig. 17.

in the brightness temperature. This is due to the sharp transition in the neutral fraction (Fig. 4).

The ionized fraction (Fig. 14) and spin temperature profile (Fig. 18) are also reflected in the brightness temperature in the case of stars as in Fig. 20. The maximum of the brightness temperature has a typical value between 20 and 30 mK for all redshifts but the negative wing spans different ranges depending on the redshift.

An interesting observation is that the maximum value of T_b remains the same throughout the mass range. The reason being that in all cases T_s is driven far away from T_{CMB}, such that the term $(1 - \frac{T_{CMB}}{T_s})$ in equation (27) approximates to unity thus removing the dependence of T_b on T_s. As a consequence of this, we also see that the brightness temperature does not change considerably during the dorment period of the quasar. Fig. 13 shows ionized fraction and temperature profile after the quasar has been switched off. But the ionized fraction is still low ($\approx 10^{-4}$) in the inner regions of the I-front, and the temperature is considerably high. Thus, the brightness temperature profile essentially remains the same.

Zaroubi & Silk (2005) have found that for power-law sources like miniqsos the brightness temperature has an extended feature in the transition from the ionized to neutral IGM. This feature has the same order of magnitude of the one found here (see Fig. 19). However, it should be noted that the origin of this feature in both cases is completely different. While in Zaroubi & Silk (2005), the extended feature is produced by the ionization–recombination balance of HE photons; here, the origin of this feature is in the heating not ionization pattern around these sources, also caused by HE photons. As Fig. 4 shows the neutral fraction of hydrogen changes abruptly at the I-front location, namely, we here show that the equilibrium
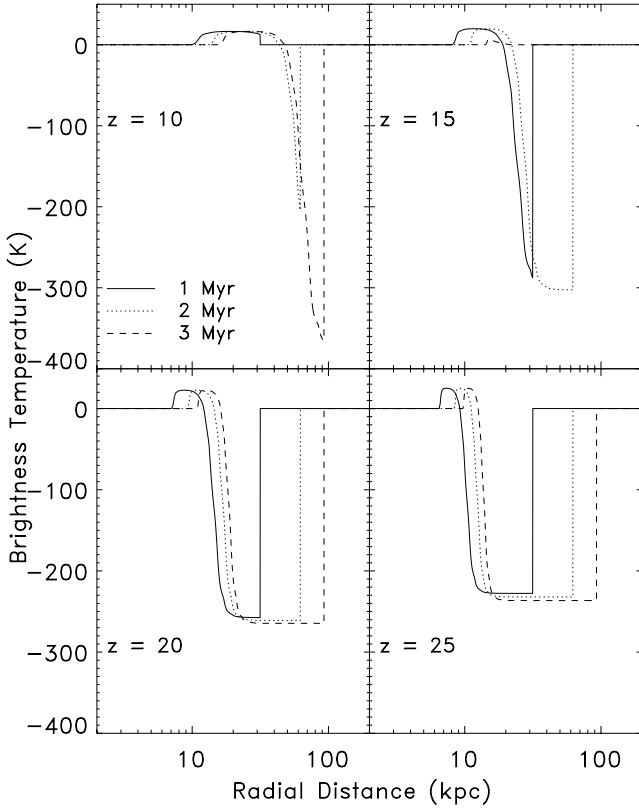
Figure 20. Brightness temperature calculated for the spin temperatures of the star shown in Fig. 18. Assumption has been made that the spin temperature remains coupled to the kinetic temperature for a radius 'ct'.

assumption of Zaroubi & Silk (2005) is never attained during the miniqso lifetime.

6.4 Observability with future telescopes

As mentioned before, there are several interferometric radio telescopes underway to measure the 21-cm signature of the EoR. It would be of interest to investigate into the possibility measuring directly the topology of the 21 cm through the brightness temperature. This, of course, depends on the angular resolution that measures the topology on the sky and the frequency resolution that will provide the depth information. We look into these aspects in the context of LOFAR and SKA measuring the 21-cm signal from redshift of 10. LOFAR[10] will have an angular resolution of about 3–5 arcmin and a spectral resolution of 1 MHz. This would correspond to a physical size on the sky of ≈1.4 and ≈5 Mpc in depth. On the other hand, SKA with an angular resolution of about 1 arcmin (Carilli & Rawlings 2004) would correspond to ≈0.5 Mpc on the sky. The spectral resolution for the EoR experiment would more or less remain the same to beat other noise effects. In the light of these rough estimates, we realize that it would be unlikely for LOFAR to see individual sources, although once the 'bubbles' start merging the sizes may become comparable. But SKA, in principle, should be able to resolve at least the relatively big bubbles of the order of 100 kpc easily.

7 SUNYAEV–ZE'LDOVICH EFFECT

Possibilities of observing the thermal and kinetic SZ effect during the EoR had been first investigated by Aghanim et al. (1996) and more recently by Iliev et al. (2007). A hot ball of ionized gas around first stars or miniqsos resembles the classic case of clusters at lower redshifts in which the SZ effect is observed today. Thus, looking for signs of reionization through the SZ effect is an obvious next step. A spin-off of the simulations of the ionization and heating of the IGM by miniqsos is the estimation of their contribution to the SZ effect. Both, the thermal and kinetic SZ effects have been considered.

For these simulations, we start at z of 20 with two seed black hole masses, 10^3 and 10^4 $M_{\odot}$. These two cases are explored in order to reach, through accretion, masses of quasars observed at a redshift of 6 by the Sloan Digital Sky Survey (SDSS). The black holes are allowed to grow in time according the following equation:

$$M(t) = M_0 \exp(f_{duty}t/t_E), \qquad (27)$$

where $M(t)$ is the mass of the black hole at time 't', f_{duty} is the duty cycle of the black hole and t_E is the time-scale of growth which is around $41 \times (\epsilon_{rad}/0.1)$ Myr. The radiation efficiency of ϵ_{rad} was set to 0.05 (Loeb 2006). We assumed a duty cycle of 30 per cent.

First objects are formed in regions that are overdense with respect to the IGM. Thus, we ran the above simulations for a density that is 10 times the mean IGM density at that epoch.

(i) *Thermal SZ effect.* Hot electrons transfer energy to the CMB photons via inverse Compton scattering, redistributing the photons in the spectrum generally towards higher energy (Sunyaev & Ze'ldovich 1972, 1980). The temperature fluctuation is thus given by

$$\frac{\Delta T}{T} = -2\frac{k_b\sigma_T}{m_e c^2} \int_0^R T_e(t;l)n_e(t;l)\,dl, \qquad (28)$$

where T_e, m_e and n_e are the electron's temperature, rest mass and density, respectively. σ_T is the Thomson cross-section and R is the radius of the ionized region. T_e and n_e are the functions of the radius and time after the quasar was switched on. All parameters required to compute equation (29) have been obtained from the simulation.

The SZ effect is the line-of-sight integral of the electron pressure. In order to estimate the effect, we considered the profiles of the temperature and the ionized fraction to be spherically symmetric and then projected the effect on to the plane of the sky. Fig. 21 shows the temperature fluctuations resulting from the black hole model mentioned above. Results are plotted for different redshifts along with their corresponding masses, down to a redshift of 6. All
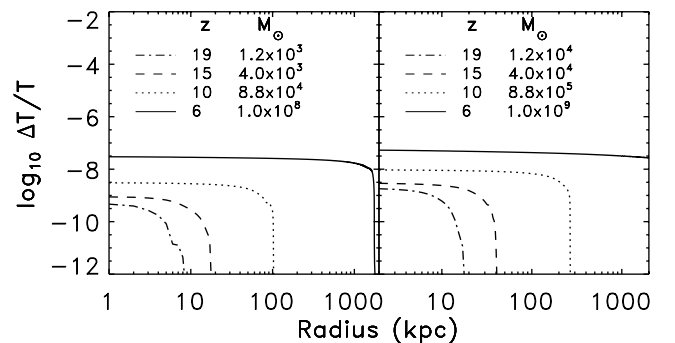

Figure 21. *Thermal SZ effect:* radial profile of temperature fluctuation $\frac{\Delta T}{T}$ for seed black hole masses 10^3 and 10^4 $M_{\odot}$ beginning at redshift $z = 20$ is shown. The different lines correspond to particular redshifts as indicated in figure. Corresponding mass according to equation (28) is shown.
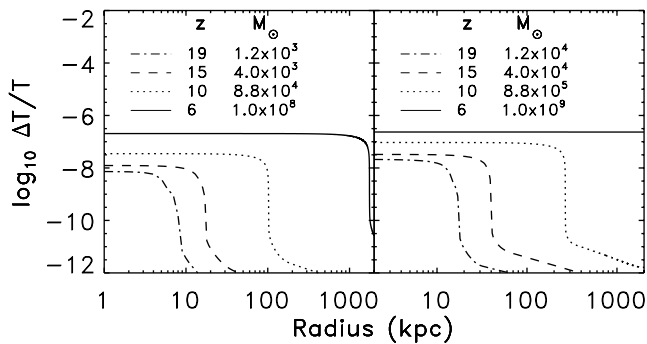
Figure 22. *Kinetic SZ effect:* radial profile of temperature fluctuation $\Delta T/T$ for the same model as in Fig. 21.

of them end at a redshift of 6 with masses comparable to the black hole masses estimated for the SDSS high-redshift quasars (Fan et al. 2003, 2006). Massive miniqsos can cause temperature fluctuations at high redshifts of the order of 10^{-7} K.

(ii) *Kinetic SZ effect*. Apart from the thermal SZ effect, there is also the possibility of observing these large ionized bubbles through the kinetic SZ-effect. Peculiar Motion of an ionized bubble with respect to the background leads to an additional change of radiation temperature in its direction, because of the finite optical depth associated with the bubble (Sunyaev & Ze'ldovich 1972). The average anisotropy associated with an ionized bubble is given by

$$\frac{\Delta T}{T} = \frac{2}{3}\frac{v_r}{c}\int_0^R 2\sigma_T n_e(t; l)\,dl, \qquad (29)$$

where v_r is the radial component of the peculiar velocity of the ionized bubble. The electron density $n_e(t; l)$ is given by the simulation and the radial component of the velocity dispersion is computed in the limit of linear theory and is given by

$$v_r(z) = v_r(0)(1 + z)^{-1/2}, \qquad (30)$$

where $v_r(0)$ is velocity dispersion at redshift zero fixed at $600\,\mathrm{km\,s^{-1}}$. The temperature fluctuation as a result of the kinetic SZ effect (equation 30) is shown as a function of the radial distance from the source in Fig. 22. Again, as for the previous case, we assumed spherical symmetry. The kinetic SZ effect is in fact larger in magnitude than thermal SZ effect, making it easily visible on the temperature maps of *Planck*. Therefore, if the sizes and temperatures of these early ionized bubbles are of the same order of magnitude predicted here, then the SZ effect is an important and independent probe of the impact of early sources on the reionization history that could be observed in the near future.

8 SUMMARY AND CONCLUSIONS

In this paper, a one-dimensional RT code has been developed in order to study in detail the influences of primordial black holes and Pop III stars on their surrounding environment. We have shown, in agreement with many other authors, that black holes and/or Pop III stars have the potential to have been the primary source of ionization. Although the ionized regions around typical black holes and Pop III stars are not shown to be convincingly different modulo the resolution of the telescopes like LOFAR, the heating around these two sources do have a significantly different profile. This in turn is reflected in the spin temperature of the system, which then directly translates into the brightness temperature measured by the radio telescope.

Spin temperatures are coupled to the kinetic temperature either through collisions or through Lyα pumping. Strengths of these coupling terms are studied as a function of the radial distance from the source. Lyα photons do couple the spin temperature efficiently to the kinetic temperature hence making the brightness temperature insensitive to the background CMB, at least for a substantial distance ($\approx$2–3 Mpc) away from the source.

Recombination time-scales are orders of magnitude lower than that of ionization. Therefore, an H II bubble remains ionized for a long period after the source of radiation has been switched off. Also the temperature remains largely unchanged for a significant fraction of Hubble time since cooling processes typically involve two body interaction that increase the time-scales involved. Interestingly for miniqsos, a marginal increase in the ionized bubble after the switching off of the central ionizing source is observed. Collisional ionizations are the dominant cause of this phenomenon which is therefore relatively less in stars because of the lack of HE X-ray photons which heats up the environment significantly hence boosting the collisional ionizations.

For miniqsos with a hard spectrum that lacks the UV part of the spectrum, we observe an excess of H I fraction as a function of radius just before the main ionization front. This is interpreted as a result of the interplay between the increase in He II and decrease in He III, which increase the H I recombination rate, on the one hand and the decrease in the photon flux as a function of radius on the other. This interpretation is supported by the weakening of the H I excess feature as a function of black hole mass. This phenomenon is not observed in miniqsos with spectrum that has UV photons, which is due to the ionization efficiency of these photons.

The results of the IGM heating around miniquasars have also been compared to the analytical approach of Zaroubi et al. (2007). Results shown in Fig. A1 demonstrate that the analytical solutions, while in agreement to within an order of magnitude, underestimate the kinetic temperature away from the centre by roughly a factor of up to 5. The difference in the results is due to the helium species cross-sections are not being fully accounted for in the analytical approach. In fact, in order for the heating to be accurately calculated one needs an exact knowledge of the abundance of each of the hydrogen and helium species averaged over their evolution history until the point in time in which one is interested and such detailed knowledge could not be obtained with the analytical approach.

Also, the thermal and kinetic SZ effects around these quasars were studied. Two cases are considered in which mass growth of the black hole is incorporated such that it winds up with 10^8 and $10^9\,\mathrm{M_\odot}$ black holes at redshifts close to six. The estimated values for the temperature fluctuations are within the sensitivies of the future mission like *Planck*.

We conclude that the brightness temperature which in turn reflects the underlying ionization and heating around a source is sensitive to many factors: the spectral energy distribution of the source, range of energies spanned by the photons of these sources, their clustering properties, the photon escape fraction, the redshifts at which the sources turn-on, their lifetimes, and many other complex feedback mechanisms, to name a few that will influence the brightness temperature, which is the observable we are after. Thus, in order to span this large parameter space, a one-dimensional RT code is necessary.

An important next step for the RT code described here is to include line emissions and absorptions, especially that of the Lyα line, in the RT equations. We will also incorporate the rate equation for molecular hydrogen and its various states.

Finally, in the near future, we plan to incorporate the results of this study into the output of *N*-body simulations. Such an approach

will allow us to produce quick 21-cm maps of the EoR, which then will be used in conjunction with the simulations of galactic and extragalactic foregrounds, ionospheric models and LOFAR specific instrument responses to generate 'dirty maps' of the EoR.

REFERENCES

Abel T., Wise J. H., Bryan G. L., 2007, ApJ, 659, L87
Aghanim N., Desert F. X., Puget J. L., Gispert R., 1996, A&A, 311, 1
Allison A. C., Dalgarno A., 1969, ApJ, 158, 423
Barkana R., Loeb A., 2001, Phys. Rep., 349, 125
Begelman M. C., Volonteri M., Rees M. J., 2006, MNRAS, 370, 289
Benson A. J., Sugiyama N., Nusser A., Lacey C. G., 2006, MNRAS, 369, 1055
Bharadwaj S., Ali S. S., 2005, MNRAS, 356, 1519
Bromm V., Kudritzki R. P., Loeb A., 2001, ApJ, 552, 464
Carilli C., Rawlings S., 2004, preprint (astro-ph/0409274)
Carilli C. L., Gnedin N., Furlanetto S., Owen F., 2004, New Astron. Rev., 48, 1053
Chen X., Miralda-Escude J., 2006, preprint (astro-ph/0605439)
Chuzhoy L., Alvarez M. A., Shapiro P. R., 2006, ApJ, 648, L1
Ciardi B., Madau P., 2003, ApJ, 596, 1
Ciardi B., Ferrara A., White S. D. M., 2003, MNRAS, 344, L7
Dijkstra M., Haiman Z., Loeb A., 2004, ApJ, 613, 646
Dijkstra M., Haiman Z., Rees M. J., Weinberg D. H., 2004, ApJ, 601, 666
Dopita M. A., Sutherland R. S., 2003, adu.book
Elvis M. et al., 1994, ApJS, 95, 1
Fan X. et al., 2003, ApJ, 125, 1649
Fan X. et al., 2006, AJ, 131, 1203
Field G. B., 1958, Proc IRE, 46, p. 240
Fukugita M., Kawasaki M., 1994, MNRAS, 269, 563
Furlanetto S. R., Loeb A., 2002, ApJ, 579, 1
Furlanetto S. R., Zaldarriaga M., Hernquist L., 2004a, ApJ, 613, 16
Furlanetto S. R., Zaldarriaga M., Hernquist L., 2004b, ApJ, 613, 1
Hogan C. J., Rees M. J., 1979, MNRAS, 188, 791
Iliev I. T., Scannapieco E., Martel H., Shapiro P. R., 2003, MNRAS, 341, 81
Iliev I. T. et al., 2006, MNRAS, 371, 1057
Iliev I. T., Pen U.-L., Bond J. R., Mellema G., Shapiro P. R., 2007, ApJ, 660, 933
Jones B. J., Wyse R. F. G., 1985, A&A, 149, 144
Kitayama T., Yoshida N., Susa H., Umemura M., 2004, ApJ, 613, 631
Kuhlen M., Madau P., 2005, MNRAS, 363, 1069
Kuhlen M., Madau P., Montgomery R., 2006, ApJ, 637, L1
Laor A., Fiore F., Elvis M., Wilkes B. J., McDowell J. C., 1997, ApJ, 477, 93
Liszt H., 2001, A&A, 371, 698
Loeb A., 2006, preprint (astro-ph/0603360)
Madau P., Efstathiou G., 1999, ApJ, 517, L9
Madau P., Meiksin A., Rees M. J., 1997, ApJ, 475, 429
Mellema G., Iliev I. T., Alvarez M. A., Shapiro P. R., 2006, New Astron., 11, 374
Nusser A., 2005, MNRAS, 359, 183
Press W. H., Teukolsky S. A., Vetterling W. T., Flannery B. P., 1992, Numerical Recipes in C. The Art of Scientific Computing. Cambridge Univ. Press, Cambridge
Ricotti M., Ostriker J. P., 2004a, MNRAS, 350, 539.
Ricotti M., Ostriker J. P., 2004b, MNRAS, 352, 547

Rhook K. J., Haehnelt M. G., 2006, MNRAS, 373, 623
Sazonov S. Y., Ostriker J. P., Sunyaev R. A., 2004, MNRAS, 347, 144
Schaerer D., 2002, A&A, 382, 28
Scott D., Rees M. J., 1990, MNRAS, 247, 510
Shapiro P. R., Giroux M. L., 1987, ApJ, 321, L107
Shaver P. A., Windhorst R. A., Madau P., de Bruyn A. G., 1999, A&A, 345, 380
Smith F. J., 1966, Planet. Space Sci., 14, 929
Spaans M., Silk J., 2006, ApJ, 652, 902
Spergel D. N. et al., 2007, ApJS, 170, 37
Shull J. M., van Steenberg M. E., 1985, ApJ, 298, 268
Sunyaev R. A., Ze'ldovich Y. B., 1972, CoASP, 4, 173
Sunyaev R. A., Zeldovich I. B., 1975, MNRAS, 171, 375
Sunyaev R. A., Ze'ldovich I. B., 1980, MNRAS, 190, 413
Tozzi P., Madau P., Meiksin A., Rees M. J., 2000, ApJ, 528, 597
Vanden Berk D. E. et al., 2001, AJ, 122, 549
Verner D. A., Ferland G. J., Korista K. T., Yakovlev D. G., 1996, ApJ, 465, 487
Vignali C., Brandt W. N., Schneider D. P., 2003, AJ, 125, 433
Volonteri M., Lodato G., Natarajan P., 2008, MNRAS, 383, 1079
Whalen D., Abel T., Norman M. L., 2004, ApJ, 610, 14
Wouthuysen S. A., 1952, AJ, 57, 31
Wyithe J. S. B., Loeb A., 2002, ApJ, 581, 886
Wyithe S., Loeb A., 2003, ApJ, 588, L69
Wyithe J. S. B., Loeb A., 2004, ApJ, 610, 117
Zaldarriaga M., Furlanetto S. R., Hernquist L., 2004, ApJ, 608, 622
Zaroubi S., Silk J., 2005, MNRAS, 360, L64
Zaroubi S., Thomas R. M., Sugiyama N., Silk J., 2007, MNRAS, 375, 1269
Ze'ldovich Y. B., Sunyaev R. A., 1969, Ap&SS, 4, 301
Zygelman B., 2005, ApJ, 622, 1356

APPENDIX A: ANALYTICAL APPROXIMATION

A number of papers have outlined analytical approximations for the ionized fraction and heating of the IGM by miniquasars (cf. Madau et al. 1997; Zaroubi et al. 2007). In order to test the validity of these analytical solutions, we compare such solution with the RT simulations for 100 and $10^4\,M_\odot$ black hole masses at z of 20 and 10 and with a lifetime of 3 and 10 Myr. Here, we follow the analytical equations of Zaroubi et al. (2007) who calculate the ionization species by solving the following ionization–recombination equilibrium equation:

$$\alpha_{\mathrm{H\,I}}^{(2)} n_{\mathrm{H}}^2 (1 - x_{\mathrm{H\,I}})^2 = \Gamma(E; r)\, n_{\mathrm{H}} x_{\mathrm{H\,I}} \left(1 + \frac{\sigma_{\mathrm{He}}}{\sigma_{\mathrm{H}}} \frac{n_{\mathrm{He}}}{n_{\mathrm{H}}}\right), \tag{A1}$$

where $\Gamma(E; r)$ is the ionization rate per hydrogen atom for a given photon energy at distance r from the source. Γ is calculated as a function of r:

$$\Gamma(E; r) = \int_{E_0}^{\infty} \sigma(E) \mathcal{N}(E; r) \frac{\mathrm{d}E}{E}. \tag{A2}$$

$\alpha_{\mathrm{H\,I}}^{(2)}$ is the recombination cross-section to the second excited atomic level and has the value $2.6 \times 10^{-13} T_4^{-0.85}\,\mathrm{cm^3\,s^{-1}}$, with T_4, the gas temperature in units of 10^4 K. For this calculation, they assume $T = 10^4$ K. Although it is not very accurate, gives a lower limit on the recombination cross-section, $\alpha_{\mathrm{H\,I}}^{(2)}$ (in neutral regions, atomic cooling prevents the gas from having a higher temperature).

Similarly, the heating rate $\mathcal{H}(r)$ is calculated as a function of the radial distance r using

$$\mathcal{H}(r) = f n_{\mathrm{H}} x_{\mathrm{H\,I}} \int_{E_0}^{\infty} \sigma(E) \mathcal{N}(E; r)\, \mathrm{d}E, \tag{A3}$$

where f is the fraction of the absorbed photon energy that goes into heating through collisional excitations of the surrounding material

(Shull & van Steenberg 1985). The function f is fitted in the paper by Shull & van Steenberg (1985) with the following simple fitting formula: $f = C\,[1 - (1 - x^a)^b]$, where $C = 0.9771, a = 0.2663$ and $b = 1.3163$ and $x = 1 - x_{\mathrm{HI}}$ is the ionized fraction. This fitting function is valid in the limit of high photon energies, an appropriate assumption for the case at hand. The fitting formula is modified by imposing a lower limit of 11 per cent for the fraction of energy that goes into heating as the proposed fitting formula does not work well at ionized hydrogen fractions smaller than 10^{-4}, and $\sigma(E)$ is the cross-section combining that of hydrogen and helium in the following manner:

$$\sigma(E) = \sigma_{\mathrm{H}}(E) + \frac{n_{\mathrm{He}}}{n_{\mathrm{H}}}\sigma_{\mathrm{He}}(E) = \sigma_1 \left(\frac{E_o}{E}\right)^3. \tag{A4}$$

Here, σ_1 is a smooth function of energy. The temperature of the IGM due to this heating is determined by the following equation (Madau et al. 1997; Zaroubi et al. 2007):

$$\frac{3}{2}\frac{n_{\mathrm{H}}k_b T_{\mathrm{kin}}(r)}{\mu} = \mathcal{H}(r)t_{\mathrm{q}}. \tag{A5}$$

Here, T_{kin} is the gas temperature due to heating by collisional processes, k_b is the Boltzmann constant, μ is the mean molecular weight and t_{q} is the miniquasar lifetime. This equation assumes that the heating rate due to the absorption of X-ray photons during the miniquasar lifetime is constant. Given the miniquasars lifetime of 3 and 10 Myr, and Hubble time at the redshifts we are interested in, cool-
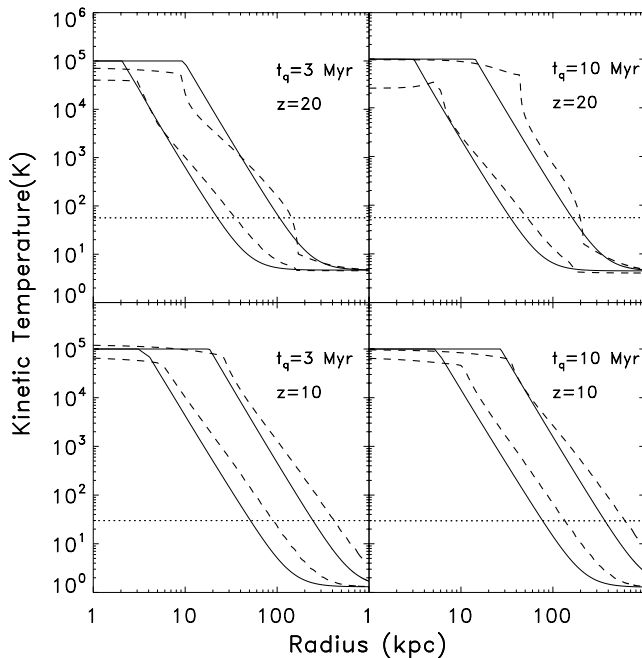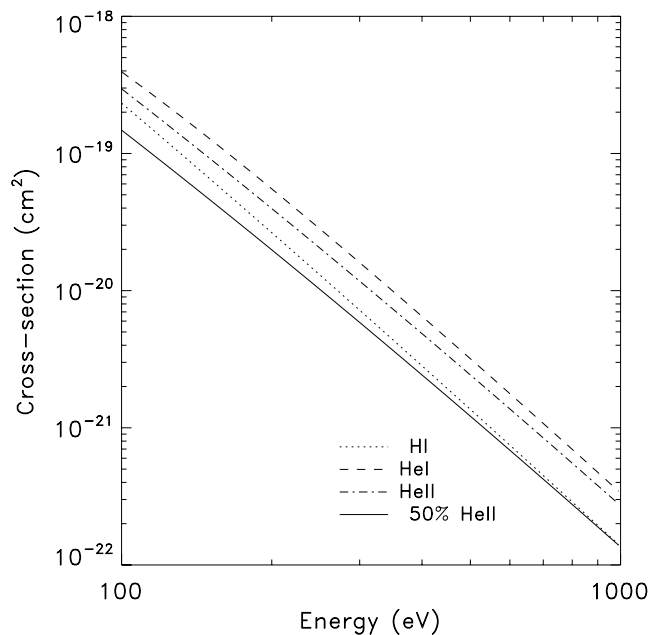

Figure A2. Figure shows the cross-sections (Verner et al. 1996) of neutral hydrogen, neutral helium and singly ionized helium, all waited by their abundances in the mean IGM. Overplotted is the also the 50 per cent singly ionized helium, i.e. all hydrogen has been ionized and 50 per cent of all helium is completely ionized.

ing due to the expansion of the Universe can be safely neglected. A 10^5 K cut-off on the gas kinetic temperature due to atomic cooling is imposed. Fig. A1 shows the kinetic temperature profiles for the four cases namely, redshifts of 20 and 10 and lifetimes of 3 and 10 Myr.

Although the figure shows an overall agreement between the simplistic analytical model and the full RT numerical solution, the analytical approach underestimates the heating by a factor of roughly 3–5 in the outer radii. The reason for this is that the helium cross-section is accounted for in the analytical approach (see equation A4) in a very incomplete fashion whereby the heating stops as soon as hydrogen is completely ionized (equation A3). In reality, this is not the case as heating by HE photons will continue until also He is fully ionized. Fig. A2 shows the cross-sections of neutral hydrogen (dotted line), completely neutral helium (dashed line), singly ionized helium (dot–dashed line) all weighted by their abundances. Overplotted on this is the case in which all hydrogen and half of all helium has been completely ionized (50 per cent He II case). At HEs, like the spectrum of the miniqso under discussion, even this fraction of singly ionized helium provides a substantial cross-section that can capture the photon and convert its energy to heat. Interestingly, looking at Figs 6 and 7 in conjunction with Figs 8 and 9 around a radial distance of 20–30 kpc reveals that there is a correlation between the increase in temperature and the corresponding increase in the singly ionized helium species.

Figure A1. Each panel in this figure shows a comparison between the model of Zaroubi et al. (2007) and the results of the spherically symmetric RT code applied to black hole masses, 100 and 10 000 M$_\odot$ with the same spectral energy distribution. The analytical calculation is represented by the solid line and that obtained from the RT code is represented by the dashed line. The different panels correspond to different values of redshift and quasar lifetime 't_{q}'.

This paper has been typeset from a TEX/LATEX file prepared by the author.